TITLE

Active zone compaction for presynaptic strength

AUTHORS

Achmed Mrestani[1], Philip Kollmannsberger[2], Martin Pauli[1,6], Felix Repp[1,2,6], Robert J. Kittel[1,3,4], Jens Eilers[4], Sören Doose[5], Markus Sauer[5], Anna-Leena Sirén[6], Manfred Heckmann[1*], Mila M. Paul[1*]

[1] Institute for Physiology, Department of Neurophysiology, Julius-Maximilians-University Würzburg, D-97070 Würzburg, Germany

[2] Center for Computational and Theoretical Biology, Julius-Maximilians-University Würzburg, D-97074 Würzburg, Germany

[3] Institute of Biology, Department of Animal Physiology, Leipzig University, D-04103 Leipzig, Germany

[4] Carl-Ludwig-Insitute for Physiology, Leipzig University, D-04103 Leipzig, Germany

[5] Department of Biotechnology and Biophysics, Julius-Maximilians-University Würzburg, D-97074 Würzburg, Germany

[6] Department of Neurosurgery, University Hospital of Würzburg, D-97080 Würzburg, Germany

[*] Correspondence should be adressed to M.H. (heckmann@uni-wuerzburg.de) and M.M.P. (mila.paul@uni-wuerzburg.de)

ABSTRACT

Synaptic plasticity is considered to underly information processing and memory formation in the brain and stabilization of neurotransmission during plasticity likely includes reorganization of active zones (AZs).

Here, we used localization microscopy and hierarchical density-based spatial clustering to probe AZ architecture at the *Drosophila melanogaster* neuromuscular junction. We observed distinct arrangements of the scaffold protein Bruchpilot (Brp) at AZs of high release probability type Is and low release probability type Ib boutons. Most remarkably, Brp proteins at type Is AZs were arranged more compact than at type Ib AZs. To ascertain whether adaptations of the AZ scaffold also occur in response to short-term demands, we used philanthotoxin (PhTx) to induce acute homeostatic plasticity. PhTx decreased AZ size, the distance between Brp subclusters and the AZ center, leading to compaction of the Brp scaffold. These changes only occurred at type Ib but not type Is AZs which, already compact, did not undergo structural rearrangement. In summary, our data describe a molecular compaction of the AZ scaffold reflecting the functional demands at high release probability synapses and during an acute homeostasic challenge.

INTRODUCTION

Synapses are complex nanomachines responsible for integration and processing of information. Their architecture and function are optimized for fast and reliable performance (Atwood and Karunanithi, 2002; Taschenberger et al., 2002; Neher and Brose, 2018), however, the structural correlate of synaptic plasticity remains elusive. In the mammalian cerebellum, Purkinje cells receive two different glutamatergic inputs (Palay and Chan-Palay, 1974). Phasic climbing fibers exhibit a higher release probability of about 40 %, whereas tonic parallel fibers show a lower release probability of about 20 % (Dittman et al., 2000; Valera et al., 2012; Schmidt et al., 2013). However, ultrastructural synaptic organization appears to be similar despite smaller mitochondria and larger synaptic vesicles in climbing fibers (Palay and Chan-Palay, 1974; Xu-Friedman et al., 2001).

In *Drosophila melanogaster* two functionally distinct motorneurons form glutamatergic neuromuscular junctions (NMJs, Karunanithi et al., 2002). Phasic type Is boutons show higher release probabilities and generate large quanta (Kurdyak et al., 1994; Karunanithi et al., 2002; Lu et al., 2016; Newman et al., 2017), whereas tonic type Ib boutons show moderate release probability and generate small quanta. Paralleling the findings in the cerebellum, type Is boutons contain larger synaptic vesicles and less mitochondria and release more glutamate per ATP molecule leading to a more energy-efficient design compared to type Ib boutons (Atwood at al., 1993; Lu et al., 2016). Yet again, little is known about the differences in molecular architecture which contribute to the functional differentiation in release probability and synaptic strength.

The above described differentiation is essentially mediated by the presynapse and likely involves distinct protein arrangement at presynaptic active zones (AZs). The cytomatrix at the active zone (CAZ) consists of an organized set of proteins (Südhof, 2012). Large α-helical coiled-coil proteins of the ELKS/CAST family are crucial for the regulation of synaptic transmission (Held et al., 2016; Dong et al., 2018). In *Drosophila* the ELKS/CAST homolog Bruchpilot (Brp) is essential for synchronous glutamate release and its amount was shown to correlate with release probability and structural synaptic differentiation (Kittel et al., 2006; Ehmann et al., 2014; Peled et al., 2014; Paul et al., 2015; Akbergenova et al., 2018). Brp is a major AZ scaffold protein responsible for clustering of presynaptic calcium channels close to release sites creating a proper

molecular environment for fast and precise neurotransmitter release (Kittel et al., 2006; Held and Kaeser, 2018). Whereas the Brp N-term was mapped in membrane-proximity, its C-term covers an area of about 0.1 µm^2, localizes about 155 nm above the postsynaptic receptors (Fouquet et al., 2009; Liu et al., 2011) and is important for tethering of synaptic vesicles (Hallermann et al., 2010). Remarkably, Brp is distributed heterogeneously within the AZ forming about 15 subclusters of 1.6 x 10^{-3} µm^2 size (Ehmann et al., 2014).

Alterations in protein number contribute to synaptic differentiation and plasticity. This is well established for receptor channels in postsynaptic densities (Tang et al., 2016). Less clear is to what extend presynaptic protein number changes contribute to plasticity. Imaging Brp and other AZ components using confocal and STED microscopy provided evidence for an increase in AZ area and cluster numbers in acute and chronic homeostatic plasticity (Weyhersmüller et al., 2011; Goel et al., 2017; Böhme et al., 2019). We suggest that beside an increase in absolute protein numbers per AZ, local protein rearrangements leading to alterations in synaptic strength are conceivable. To address this hypothesis, we performed localization microscopy of AZs in phasic and tonic presynapses at the NMJ and induced presynaptic homeostatic plasticity as a model for acute changes in release (Davis and Müller, 2015). Hierarchical density-based spatial clustering (HDBSCAN) enabled unbiased analysis of our datasets. We identified striking differences in AZ scaffold organization with more compact Brp arrangement, increased molecular density and narrower positioning of AZ subclusters in high release probability, phasic type Is boutons compared to low probability, tonic type Ib boutons. Furthermore, we observed similar changes following induction of acute presynaptic plasticity only in tonic type Ib boutons. In summary, our data suggest AZ compaction to be a structural correlate of enhanced synaptic transmission in synaptic differentiation and homeostatic plasticity.

MATERIAL AND METHODS

Fly stocks

Flies were raised on standard cornmeal and molasses medium at 25 °C. *Drosophila melanogaster* wildtype strain w^{1118} (Bloomington *Drosophila* Stock Center) male 3rd instar larvae were used for experiments.

Philanthotoxin treatment and and larval preparation

Philanthotoxin 433 tris (trifluoroacetate) salt (PhTx, P207 Sigma) was dissolved in dimethyl sulfoxide (DMSO) to obtain a stock solution of 4 mM and stored at -20 °C. For each experiment, the respective volume was further diluted with freshly prepared haemolymph-like solution (HL-3, Stewart et al., 1994) to a final PhTx concentration of 20 µM in 0.5 % DMSO. Control experiments were performed with the same DMSO concentration in HL-3. PhTx treatment of semi-intact preparations was performed essentially as described previously (Frank et al., 2006). In brief, larvae were pinned down in calcium-free, ice-cold HL-3 at the anterior and posterior endings, followed by a dorsal incision along the longitudinal axis. Larvae were incubated in 10 µl of 20 µM PhTx in DMSO for 10 minutes at room temperature (22 °C). Following this incubation time, PhTx was replaced by HL-3 and larval preparations were completed, followed by fixation and staining.

Fixation, staining and immunofluorescence

After PhTx treatment and dissection, larvae were fixed with 4 % paraformaldehyde in phosphate buffered saline (PBS) for 10 minutes and blocked for 30 minutes with PBT (PBS containing 0.05 % Triton X-100, Sigma) including 5 % natural goat serum (Dianova). Primary antibodies were added for overnight staining at 4 °C. After two short and three long (20 min each) washing steps with PBT, preparations were incubated with secondary antibodies for 3 hours at room temperature, followed by two short and three long washing steps with PBT. Preparations were kept in PBS at 4 °C until imaging. All data were obtained from NMJs formed on abdominal muscles 6/7 in segments A2 and A3, except data for Supplementary Figure 4, which were obtained from NMJs formed on abdominal muscle 4 in segments A2-A4. Directly compared data (e.g. Figure 1C) were obtained from larvae stained in the same vial and measured in one imaging session.

_d_STORM (_direct_ stochastic optical reconstruction microscopy)

Super-resolution imaging of the specimen was performed essentially as previously reported (Ehmann et al., 2014; Paul et al., 2015). Preparations were incubated with monoclonal antibody (mAb) Brp^{Nc82} (1:100, Antibody Registry ID: AB_2314866, Developmental Studies Hybridoma Bank) and secondary antibody goat α-mouse $F(ab')_2$ fragments labelled with Alexa Fluor647 (1:500, A21237, Thermofisher). Boutons were visualized using Alexa Fluor488 conjugated goat α-horseradish-peroxidase antibody (α-hrp, 1:250, Jackson Immuno Research). After staining, larval preparations were incubated in 100 mM mercaptoethylamin (MEA, Sigma-Aldrich) buffer in PBS, pH 7.8 to 7.9 to allow reversible switching of single fluorophores during data acquisiton (van de Linde et al., 2008). In all experiments, images were acquired using an inverted microscope (Olympus IX-71, 60x, NA 1.49, oil immersion) equipped with a nosepiece-stage (IX2-NPS, Olympus). 647 nm (F-04306-113, MBP Communications Inc.) and 488 nm (iBEAM-SMART-488-S, Toptica) lasers were used for excitation of Alexa Fluor647 and Alexa Fluor488, respectively. Laser beams were passed through clean-up filters (BrightLine HC 642/10, Semrock and ZET 488/10, Chroma, respectively) combined by a dichroic mirror (LaserMUX BS 473-491R, 1064R, F38-M03, AHF Analysentechnik) and directed onto the probe by an excitation dichroic mirror (HC Quadband BS R405/488/532/635, F73-832, AHF Analysentechnik). The emitted fluorescence was filtered with a quadband-filter (HC-quadband 446/523/600/677, Semrock) and a longpass- (Edge Basic 635, Semrock) or bandpass-filter (Brightline HC 525/50, Semrock) for the red and green channel, respectively, and divided onto two cameras (iXon Ultra DU-897-U, Andor) using a dichroic mirror (HC-BS 640 imaging, Semrock). The green channel was used to visualize individual presynaptic boutons in normal fluorescence microscopy. For the red channel, image resolution was 126 nm x 126 nm per pixel to obtain super-resolution of Brp. Single fluorophores were localized and high resolution-images were reconstructed with rapi*d*STORM (Heilemann et al., 2008; van de Linde et al., 2011; Wolter et al., 2010; Wolter et al., 2012; www.super-resolution.de). Only fluorescence spots with more than 12000 photons were analyzed and subpixel binning of 10 nm px^{-1} was applied. For visualization of representative *d*STORM measurements, reconstructed images from rapi*d*STORM with 5 nm binning were opened in FIJI (Schindelin et al., 2012) and where contrast enhanced for clarity. Localization precision (Supplementary Figure 1A) was determined with the NeNa algorithm (nearest neighbor

based analysis, Endesfelder et al. 2014), implemented in the LAMA software package (LocAlization Microscopy Analyzer; Malkusch and Heilemann, 2016). To check for homogenous illumination of the samples we analyzed and compared localization intensity of all *d*STORM measurements, (i) for the whole image, and (ii) only for analyzed regions and found no differences in A/D counts between experimental groups (Supplementary Figure 1B).

Confocal microscopy

For confocal imaging larvae were mounted in PBS and imaged using a commercial confocal laser scanning microscope (Zeiss LSM 700) equipped with an oil-immersion objective (Plan-Apochromat 63x/1.40 Oil M27). Alexa Fluor647 and Alexa Fluor488 were excited with the 639 nm and the 488 nm diode laser lines, repectively. The microscope was operated and the images were stored with ZEN 12 software (black edition, Zeiss AG). For each z-stack 7-13 slices with 200 nm axial spacing were obtained. The gain of the photomultiplier tubes was adjusted to 700 and 600 and laser power was set to 1.5 % and 1 % in red and green channels, respectively, to obtain a good signal with little photobleaching allowing subsequent *d*STORM imaging. The pinhole was set to 70.6 µm, corresponding to 1.32 Airy units in the red and 1.73 Airy units in the green channel. Images were recorded in 1024 x 1024 (lines x pixels) format with 16-bit data depth. Given an approximate resolution of 200 nm in the red channel, the pixel size, adjusting the zoom factor to 1.2, was set to about 83 nm for sufficient data sampling. Settings resulted in a pixel dwell time of 3.15 µs.

Data evaluation

Localization microscopy data were analyzed with custom written Python code (https://www.python.org/, language version 3.6) and the web-based Python interface Jupyter (https://jupyter.org/index.html). Localization tables from rapi*d*STORM were directly loaded and analyzed. Prior to the Python-based analysis the regions of interest (ROI) were masked in the reconstructed, binned images from rapi*d*STORM using FIJI (1.440, Schindelin et al., 2012). These ROIs corresponded to the terminal 6 boutons according to the α-hrp staining. In earlier work on super-resolved Brp-data, density-based spatial clustering of applications with noise (DBSCAN) was used to identify AZ subclusters (Ehmann et al., 2014). Given the parameters k and ε, DBSCAN considers a group of localizations as a cluster if there are at least k residues in a circle with radius

ε around a certain localization (Ester et al., 1996). Here, we used an improved approach called hierarchical density-based spatial clustering of applications with noise (HDBSCAN) that, in contrast, extracts the most robust clusters from a cluster hierarchy over varying ε environments that are least sensible to ε variation, i.e have the longest lifetime in the cluster tree (Supplementary Figure 2; Campello et al., 2013). The algorithm is thus more powerful for cluster detection in data with variable density. We used the Python implementation of HDBSCAN (McInnes et al., 2017; https://github.com/scikit-learn-contrib/hdbscan), which takes minimum cluster size as the main free parameter, and performed two steps of clustering with different values for minimum cluster size on our localization data: (i) to identify the AZs, and (ii) to extract the subclusters from the AZs. We explored optimal clustering parameters for the detection of active zones and varied the minimum cluster size parameter for HDBSCAN (Supplementary Figure 2F). HDBSCAN in Python takes another parameter called minimum samples. By default, this parameter is set to minimum cluster size but choosing a smaller value allows the algorithm to be less conservative, i.e. extract clusters that might be smaller than minimum cluster size but very robust in the cluster hierarchy. We decided to vary minimum samples as a constant fraction of 25 % of minimum cluster size. As expected, increasing minimum cluster size also leads to increasing cluster sizes in tendency. We visually checked the results of our cluster analyses and concluded that a minimum cluster size of 100 yields the most reliable results for AZ detection. Too high values falsely merge adjacent AZs together whereas too low values lead to fragmenting AZs into smaller clusters. However, we found that changes of AZ properties between different experimental groups were robust to varying parameters for AZ clustering (Supplementary Figure 2F). A second HDBSCAN on the individual AZ clusters was performed with minimum cluster size of 24 and a similar number of subclusters was found compared to the DBSCAN-based subcluster analysis of Ehmann et al., 2014. For our subcluster analysis, the cluster selection method was changed to ‘leaf’ clustering, which comprises a tendency to more homogenous clusters by extracting those that lie on leaf nodes of the cluster tree rather than the most stable clusters. To quantify cluster area, we computed 2D alpha shapes using CGAL (Computational Geometry Algorithms Library, https://www.cgal.org) in Python. The geometrical concept of alpha shapes can be used to calculate the shape and thus the area of a set of points. Given a finite set of points and an alpha value α, an edge of the shape is drawn between two points whenever they lie on the boundary

of a disk with radius $\alpha^{1/2}$ that does not contain any other point (Edelsbrunner and Mücke, 1994). To get the alpha shapes of the AZ clusters and AZ subclusters we choose α-values of 800 nm^2 and 300 nm^2, respectively. The subcluster center of mass (c.o.m) was calculated as mean of the x- and y-values of all localizations of the subcluster, and the AZ c.o.m as mean of its subcluster c.o.m.s. To estimate the distance of subcluster c.o.m. from AZ c.o.m. the Euclidean distance of these points was computed and divided by the square root of the respective AZ area to obtain the area-normalized distance. For evaluation of Brp cluster circularity, the ratio of the Eigenvalues of each cluster was computed, where 1 indicates a perfect circle and values < 1 indicate decreasing circularity (Supplementary Figure 5A). Exclusion criteria for outliers in all *d*STORM data evaluations were AZ area < 0.03 μm^2 (Ehmann et al., 2014) and > 0.3 μm^2, absolute localization counts per AZ > 8000 and mean AZ localization density > 60000 localizations per μm^2 (about 3-5-fold median). Additional exclusion criteria for type Ib neuron recordings were mean AZ localization count < 1000 and at the same time mean AZ area < 0.095 μm^2 per image, indicative of insufficient data quality. For visualization of the localization-based results (Figure 1B, Figure 2B) scatter plots were created in Python. H functions as derivatives of Ripley's K function were computed using Python package astropy (Robitaille et al., 2013) for each individual AZ and for the random poisson distribution and curves for display were averaged. The function was evaluated in nm steps for radii from 0 to 120 nm and without correction for edge effects. For nearest neighbor analyses we used scikit-learn (Pedregosa et al., 2011) and computed the mean nearest neighbor distance (NND) from the first nearest neighbor of all localizations per AZ. To simulate confocal resolution (Figure 4) localization tables from rapi*d*STORM with 5 nm binning were converted to FIJI-readable density matrices where raw integrated density corresponds to the localization count in a pixel. Images were contrast enhanced to obtain 0.1 % saturated pixels, a Gaussian filter with 150 nm standard deviation (SD) was applied and the images were scaled to a pixel size of 80 nm. Representative images for both experimental groups were chosen and only pixels in the same ROIs as described above were used for subsequent processing and analysis. Images were converted to 8-bit and the gain was adjusted by scaling all pixels in both images to the same value (the brightest of all analyzed pixels in both images was set to the maximum value of 255). Following a standard protocol for the quantification of confocal data of the *Drosophila* NMJ (Schmid et al., 2008; Weyhersmüller et al., 2011) a minimal threshold

of 50 was applied, and the 'Analyze Particles' function in FIJI was used to create individual masks from the thresholded images. The resulting masks were applied to the non-thresholded simulated confocal images to quantify AZ area as well as the mean intensity of the AZ. STED resolution in Figure 4 was simulated similarly, but a Gaussian filter with 25 nm SD was applied to the density matrices. The images had full gain in 8-bit, thus were not further scaled. Planar-oriented AZs were selected using a circular shape including a central hole for recognition. Selection was performed blinded with respect to the experimental groups. Obvious background was removed and single AZs were cut out from the whole images. AZ area and mean pixel intensity per AZ were measured with a threshold of 18 arbitrary units (a. u.; Böhme et al., 2019). Intensity maxima were extracted using the 'Find Maxima' function in FIJI with default settings and quantified per AZ. Confocal images were processed and evaluated in FIJI. Z-stacks were maximum projected and Brp spots segmented with pixel intensity thresholds of 50, 100 and 150 a. u. in 8-bit using the 'Analyze Particles' function (Figure 5A). Mean pixel intensity of resulting masks was measured in the original images. Corresponding Brp spots, extracted with 100 a. u. threshold, and Brp localization clusters were assigned manually. Only clusters that were clearly distinguishable in both confocal and *d*STORM without confluence to neighboring signal were used.

Statistics

Statistical analyses were performed with Sigma Plot 13 (Systat Software). Shapiro-Wilk was used to test normality. If data were not normally distributed, we used the non-parametric Mann-Whitney rank sum test for statistical analysis and reported data as median (25^{th}-75^{th} percentile) unless indicated otherwise (Supplementary Figure 2F). If data were normally distributed t-test was used and data were reported as mean ± SEM unless indicated otherwise (Figure 4E, G). Asterisks indicate statistical significance ($p < 0.05$) and n denotes sample number. In box plots, horizontal lines represent median, boxes quartiles and whiskers 10^{th} and 90^{th} percentiles. Scatter plots show individual data points unless indicated otherwise. Bin counts in histograms were normalized to the total number of observed events and displayed in %. Linear regression curves were fitted and Spearman correlation coefficient r and statistical significance p of correlations were evaluated in Sigma Plot. All plots were produced with Sigma Plot software and figures assembled using Adobe Illustrator (Adobe, 2015.1.1 release).

Code and data availability

The authors declare that custom written Python code and all data sets supporting the findings of this work are available from the corresponding authors.

RESULTS

To analyze the AZ nanostructure in tonic type Ib and phasic type Is boutons (Atwood et al., 1993; Kurdyak et al., 1994; Lnenicka and Keshishian, 2000; Hoang and Chiba, 2001), we employed *direct* stochastic optical reconstruction microscopy (*d*STORM, Heilemann et al., 2008; van de Linde et al., 2011) overcoming the diffraction limit of conventional light microscopy. We used a highly specific monoclonal antibody Brp^{Nc82}, mapping to the C-terminal region of the protein (Fouquet et al., 2009) that has been succesfully used to study AZ nanoarchitecture with super-resolution microscopy (Kittel et al., 2006; Ehmann et al., 2014). To test the hypothesis that differences in synaptic performance are reflected by Brp reorganization, we imaged type Ib and type Is AZs on abdominal muscles 6/7 in segments A2 and A3 of male crawling 3rd instar *Drosophila melanogaster* larvae (Figure 1A). Since Brp is the most abundant AZ scaffold protein and the Brp^{Nc82} epitope covers the spatial extent of an individual AZ, we will interpret 'Brp area' as 'AZ area' in this study. We employed a localization-based clustering algorithm HDBSCAN (Material and Methods) in custom written Python code (Figure 1B). This allowed fast, automated analysis of large data sets with several hundred AZs per experimental group and rapid analysis of their clustering. In addition, the approach facilitated rapid subgroup evaluation of large data sets (Supplementary Figure 5).

Differences of AZ nanostructure between type Ib and type Is boutons in *Drosophila* wildtype larvae

Our analysis concentrated on the first (most distal) 6 boutons of a string without further selection criteria (Paul et al., 2015). In accordance to previous work (Ehmann et al., 2014), we found that AZ area was smaller in type Is than in type Ib boutons (Figure 1C, median (25th-75th percentile) 0.088 (0.06-0.142) µm^2 and 0.106 (0.078-0.162) µm^2, respectively, $p < 0.001$). As *d*STORM allows to estimate protein numbers (Löschberger et al., 2012; Ehmann et al., 2014) we compared the number of Brp localizations per AZ in both bouton types and found fewer localizations per AZ in type Is boutons (Figure 1D, 1399 (873-2194) locs. per AZ and 1586 (1031-2369) locs. per AZ in type Is and type Ib boutons, $p < 0.001$). However, the density of Brp localizations was higher in AZs of type Is than in those of type Ib boutons (Figure 1E, 15146 (12939-17583) locs. per µm^2 and 13819 (11555-16486) locs. per µm^2, $p < 0.001$). To compare AZ shape, we quantified the circularity of Brp spots as the ratio of their Eigenvalues of the

covariance matrix (ratio between 0 and 1; 1 indicating a perfect circle taken as indication for viewing an AZ untilted, i.e. from the top, see Material and Methods) and extracted the distributions for both groups. We found that AZ circularity of type Is boutons was smaller than of type Ib boutons (Figure 1F, 0.58 (0.45-0.72) and 0.65 (0.52-0.76), respectively, $p < 0.001$). In summary, AZs of type Is boutons are smaller, comprise a higher Brp concentration and have a less circular shape than AZs of type Ib boutons.

Distinct organization of Bruchpilot subclusters in type Ib and type Is boutons

A previously published clustering algorithm (modified from Bar-On et al., 2012) revealed that Brp molecules are distributed heterogeneously within the AZ (Ehmann et al., 2014). The authors detected on average 14.5 ± 0.4 (mean ± SEM) Brp clusters per CAZ unit in type Ib boutons and calculated that ~74 % of all Brp localizations are clustered. Cluster algorithms are not suitable to decide whether a point distribution is clustered or not-clustered. Here, we used Ripley's K function and its derivatives L and H function to determine properties of spatial point patterns independently from conventional clustering algorithms (Kiskowski et al., 2009). Positive values for H(r) indicate clustering, negative values indicate dispersion or edge effcts and maximum positive values roughly correspond to the radius of putative clusters. To confirm that Brp comprises a clustered substructural organization at the AZ, we computed H functions of all localizations of individual AZs, obtained averaged curves for the whole population of type Ib and type Is AZs and compared them to the expected curves for a random Poisson distribution (Figure 2A upper panel). These curves show positive values between 1 and 58 nm and 1 and 55 nm with their maxima at 24 nm and 23 nm for type Ib and type Is AZs, respectively. This confirms clustering of Brp on a substructural level and closely matches with published size of Brp submodules (Ehmann et al., 2014). Another way to extract quantitative information from localization distributions is a nearest neighbor analysis (Szoboszlay et al., 2017), a technique successfully used previously to study structure and dynamics of AZ proteins (Glebov et al., 2017; Rebola et al., 2019). The mean nearest neighbor distance (NND) of all Brp localizations per AZ was smaller at type Is than at type Ib AZs (Figure 2A lower panel, 4.1 (3.7-4.5) nm and 4.3 (3.9-4.7) nm, $p < 0.001$) as expected for a higher protein density. We conclude that Brp arrangement in AZs of type Is and Ib neurons differs.

To further investigate whether Brp subcluster (sc.) organization is also different in the two motor inputs, we developed custom written Python code using the aforementioned HDBSCAN (Material and Methods). In addition to the determination of individual subclusters, this localization-based analysis allowed us to define a center of mass (c.o.m.) for each AZ as well as for its individual subclusters and therefore measure their specific interspaces (Figure 2B). Our analysis revealed that the number of subclusters per AZ was lower in type Is than in type Ib boutons (Figure 2C, 13 (8-20) and 14 (9-21), $p = 0.004$) and subcluster size was smaller (Figure 2D, 1.5 (1.2-1.9) x 10^{-3} µm^2 and 1.6 (1.3-2.0) x 10^{-3} µm^2, $p < 0.001$). Interestingly, whereas absolute numbers of Brp localizations (locs.) per subcluster remained unaltered (Figure 2E, 56 (50-63) locs. per sc. and 55 (50-62) locs. per sc. in type Is and type Ib boutons, $p = 0.618$), Brp localization density of an individual subcluster was higher in type Is than in type Ib AZs (Figure 2F, 37238 (31515-44125) locs. per µm^2 and 34077 (28599-39907) locs. per µm^2 in type Is and type Ib boutons, $p < 0.001$). Furthermore, the clustering algorithm defined individual c.o.m.s for each AZ, as well as for their subclusters (Figure 2B). The distance between AZ c.o.m. and subcluster c.o.m.s (referred to as 'radial distance') was compared in AZs of both bouton types and was significantly smaller in type Is boutons (Figure 2G, 114 (90-154) nm and 120 (99-156) nm in type Is and type Ib boutons, $p < 0.001$). Since AZ area was smaller in Is AZs too, we normalized this parameter to the size of the resepective AZ. This gave an inverse effect (Figure 2H, 0.39 (0.35-0.43) a. u. and 0.37 (0.34-0.40) a. u. in type Is and type Ib boutons, $p < 0.001$), which suggests a different configuration of Brp subclusters in type Is AZs. In summary, AZs of type Is boutons contain fewer subclusters, which are smaller but contain a higher density of Brp molecules, and in addition, these subclusters are located closer to the AZ center. Taken together, our data provide evidence that the higher release probability of type Is boutons might be reflected by a more compact AZ scaffold.

Acute homeostatic plasticity changes Bruchpilot organization in type Ib boutons

Next, we wanted to investigate whether differences of the AZ scaffold can also occur in response to a short-term functional demand. Thus, we studied the effect of acute presynaptic homeostasis induced by Philanthotoxin (PhTx), which is characterized by an increase in quantal content and number of release-ready vesicles (Frank et al., 2006; Weyhersmüller et al., 2011; Davis and Müller, 2015). Using *d*STORM we

analyzed AZ configuration of type Ib boutons in wildtype larvae incubated in DMSO (control, ctrl) or in PhTx (phtx, Figure 3A). AZ area was reduced in phtx larvae (Figure 3B, 0.109 (0.074-0.169) µm^2 and 0.101 (0.068-0.148) µm^2 in ctrl and phtx, p = 0.009). In addition, whereas absolute Brp localization numbers were unchanged in phtx (Figure 3C, 1532 (1007-2303) locs. per AZ and 1453 (926-2346) locs. per AZ in ctrl and phtx, p = 0.236), the molecular density of Brp was increased after PhTx treatment (Figure 3D, 13555 (11308-16236) locs. per µm^2 and 14082 (11756-17204) locs. per µm^2 in ctrl and phtx, p = 0.009). Thus, acute homeostatic plasticity induces a rearrangement of Brp within individual AZs of type Ib boutons without changing the number of Brp molecules per AZ. Previous work discovered a proximo-distal gradient along the type Ib bouton string regarding structure and function, with distal boutons containing more AZs with elevated Brp counts and glutamate release compared to proximal ones (Peled and Isacoff, 2011; Ehmann et al., 2014; Paul et al., 2015). Therefore, we aimed to explore whether the structural changes in response to PhTx treatment occur in a distinct spatial pattern within the NMJ. We performed subgroup analysis of AZs in type Ib boutons number 1-6 separately, and per definition the last bouton, i.e. the most distal one, was referred to as bouton number 1 (Figure 3E, Paul et al., 2015). Spearman correlation coefficients displayed no significant correlation between bouton number and Brp localization density in both groups (Figure 3E, r = 0.657 and p = 0.175 and r = 0.829 and p = 0.0583 in ctrl and phtx). Thus, the observed density increase occurs in all boutons along the string. These data support the conclusion that structural plasticity in acute homeostasis happens homogeneously at the NMJ and does not include differentiation between boutons of a given type Ib neuron.

To elucidate if Brp reorganization during acute homeostasis also takes place within subclusters of the AZ scaffold, we again employed the aforementioned algorithms for determination of subclusters. H functions for control and phtx revealed modular AZ structures, as described above for wildtype type Is and Ib boutons (Supplementary Figure 3A). Next, we measured nearest neighbor distances of all AZ localizations and found a decrease in phtx larvae (Supplementary Figure 3B, 4.4 (3.9-4.7) nm and 4.2 (3.8-4.6) nm in ctrl and phtx, p < 0.001). Comparison of the number of Brp subclusters per AZ detected by HDBSCAN revealed no difference between both groups (Figure 3F, 15 (10-21) and 13 (9-21) in ctrl and phtx, p = 0.084). However, subcluster area was

slightly decreased after PhTx treatment (Figure 3G, 1.7 (1.3-2.1) µm^2 and 1.6 (1.3-2.0) µm^2 in ctrl and phtx, p = 0.025). Interestingly, comparing Brp localizations per subcluster and Brp localization density in both groups yielded comparable effects as described for type Ib and type Is boutons (Figure 2): whereas absolute Brp localization numbers remained unchanged after PhTx treatment (Figure 3H, 57 (51-64) locs. per sc. and 56 (51-64) locs. per sc. in ctrl and phtx, p = 0.480), Brp localization density of an individual subcluster increased during acute homeostasis (Figure 3I, 33914 (28276-40553) locs. per µm^2 and 34290 (29464-42454) locs. per µm^2 in ctrl and phtx, p = 0.022). This increased molecular density of Brp subclusters both in strongly releasing type Is boutons as well as in PhTx-treated type Ib boutons is in line with the increase in release probability. Finally, we examined radial distances between the c.o.m. of an AZ and the subcluster c.o.m.s. Remarkably, we found that PhTx decreased radial distance (Figure 3J, 125 (102-163) nm and 116 (96-153) nm in ctrl and phtx, p = 0.003). Taken together, these data show that Brp reorganization during acute homeostasis also occurs within individual subclusters of type Ib AZs without changing the Brp amount per subcluster or per AZ.

Up to this point, data were obtained from NMJs on abdominal muscles 6/7. Some earlier studies imaged abdominal muscle 4 to analyze the effect of PhTx on AZs (Goel et al., 2017; Böhme et al., 2019). The NMJ on muscle 4 forms only type Ib boutons, which might lead to different results and also excludes the possibility to compare two motorinputs at the same NMJ. Thus, we repeated PhTx treatment, performed *d*STORM imaging of NMJs of muscle 4 and applied our cluster analysis. This yielded similar results as shown for type Ib AZs on abdominal muscles 6/7 (Supplementary Figure 4).

Subgroup analysis of AZ structure in planar view

It is arguable that the orientation of individual AZs has to be taken into account while analyzing radial distributions of molecule clusters. Thus, we used the earlier described tool in our analysis algorithm to measure Brp circularity (Figure 1F) and extracted the distributions in ctrl and phtx (Supplementary Figure 5). As AZ circularity was unaffected by PhTx (Supplementary Figure 5A, 0.64 (0.52-0.75) and 0.65 (0.52-0.77) in ctrl and phtx, p = 0.161), it appeared appropriate to analyze the whole dataset without subgroup selection. Furthermore, to address whether planar oriented AZs (i.e.

circularity closer to 1) change similarly following PhTx treatment as the whole AZ population, we investigated the relation between AZ area and circularity. Interestingly, this uncovered an inverse correlation represented by Spearman correlation coefficients (Supplementary Figure 5B, $r = -0.241$, $p < 0.001$ and $r = -0.271$ in ctrl and phtx, $p < 0.001$). We interpret that low circularity is indicative of AZs in side view or of large Brp spots that partially arise from merged AZs lying nearby in 2D projection. The latter have been referred to as double ring structures, grouped CAZ units or cluster AZs (Kittel et al., 2006; Ehmann et al., 2014; Akbergenova et al., 2018). Assuming that some structural parameters depend strongly on the orientation of the respective AZ, we analyzed AZ area and radial distance in a subsample of AZs with circularity ≥ 0.5, assuming a planar orientation (Supplementary Figure 5C). We found a pronounced decrease in AZ area (0.103 (0.075-0.149) μm^2 and 0.094 (0.068-0.135) μm^2 in ctrl and phtx, $p = 0.002$) and a similar decrease of radial distance in both groups (119 (101-148) nm and 112 (95-139) nm in ctrl and phtx, $p < 0.001$). These data indicate that Brp subcluster compaction correlates with a functional AZ state adjusted to presynaptic potentiation.

Nanoscale molecular compaction appears as increased area and intensity in confocal and STED simulations

The effect of presynaptic homeostasis on AZ structure examined with confocal and STED microscopy showed an increase of Brp spot area and intensity (Weyhersmüller et al., 2011; Goel et al., 2017; Böhme et al., 2019). Our *d*STORM measurements, however, revealed a significantly smaller AZ area but an increase of Brp localization density following PhTx treatment (Figure 3). To gain a better understanding how earlier described changes of AZ structure during acute homeostasis relate to our findings, we performed simulations of confocal spatial resolution applying a Gaussian filter of 150 nm SD and 80 nm pixel size to our original *d*STORM data (Figure 4A, B). 3D bar plots of mean pixel intensity with 80 nm bins of two example AZs in ctrl and phtx illustrate the applied thresholding level of 50 a. u. used for further quantification (Figure 4C, compare Figure 4B in Weyhersmüller et al., 2011). Analysis of AZ area and mean pixel intensity in one representative *d*STORM image per group after simulation of confocal resolution revealed an increase of both AZ parameters (Figure 4E, 0.346 (0.155-0.725) μm^2 and 0.442 (0.230-0.678) μm^2 in ctrl and phtx; mean pixel intensity (mean ± SEM): 80 ± 2 a. u. and 96 ± 3 a. u. in ctrl and phtx). In comparison, analysis of AZ area and

Brp localization density in that image in original resolution showed the decrease in AZ area and the increase of Brp localization density that was described for the whole dataset (Figure 4D, 0.127 (0.074-0.185) µm^2 and 0.101 (0.072-0.141) µm^2, 13396 (11444-15049) locs. per µm^2 and 14657 (12834-18221) locs. per µm^2 in ctrl and phtx). We conclude that intensity-based quantification with confocal resolution may lead to inverse results concerning AZ area compared to localization-based analysis. In the next step, we simulated STED resolution in the same images used before for confocal simulation and applied a Gaussian filter of 25 nm SD (Figure 4F). AZ area and mean pixel intensity were measured similarly as mentioned above, but with a threshold of 18 a. u., and intensity maxima per AZ were detected with a peak finding algorithm in FIJI. This analysis revealed an increased AZ area and mean pixel intensity, as well as a slight increase of the number of intensity maxima per AZ after induction of presynaptic homeostasis (Figure 4G, AZ area 0.08 (0.06-0.103) µm^2 and 0.089 (0.075-0.115) µm^2 in ctrl and phtx; mean pixel intensity mean ± SEM: 39 ± 1 a. u. and 53 ± 1 a. u. in ctrl and phtx; intensity maxima per AZ 3 (2-4) and 3 (3-5) in ctrl and phtx). In summary, simulation of STED resolution gives inverse results for the number of clusters per AZ matching to aforementioned findings.

Correlative imaging links increased localization density to increased confocal intensity and AZ area

To further study the correlation between localization density and the confocally measured AZ area and signal intensity suggested by our simulation, we perfomed sequential confocal-*d*STORM imaging of Brp in type Ib boutons (Figure 5A and B). Confocal data were analyzed with intensity thresholds of 50, 100 and 150 a. u. to clarify the influence thresholding has on quantification (Figure 5A). As expected, higher thresholds improved segmentation of individual Brp spots but at the same time eliminated more signal, whereas a low threshold provided best signal preservation but led to insufficient segmentation. For further quantification 100 a. u. thresholding was used. Figure 5C shows enlarged AZs overlaid in confocal and *d*STORM resolution in green, magenta and blue to mark AZ identity. Magenta and blue AZs in Figure 5Ci display areas of 0.143 µm^2 and 0.118 µm^2 in *d*STORM and localization densities of 20590 locs. per µm^2 and 14775 locs. per µm^2, respectively, with a clearly separated green AZ. Confocal imaging cannot distinguish this green AZ and, due to the high localization density of the magenta AZ, further overestimates AZ area compared to

546 *d*STORM (0.417 µm^2 and 0.171 µm^2 for the merged green and magenta AZ and the
547 blue AZ in confocal). Thresholding of confocal images can also lead to complete loss
548 of signal that is included in *d*STORM quantification (Figure 5Cii). Additionally,
549 segmentation of closely spaced AZs is superior using HDBSCAN-based quantification
550 of localization data compared to thresholding-based quantification of confocal data
551 (Figure 5Ciii). In the next step we quantified AZs of the whole dataset after correlative
552 confocal-*d*STORM imaging. Distribution of AZ area was broader in confocal
553 microscopy than in *d*STORM (Figure 5D, 0.164 (0.103-0.246) µm^2 and 0.101 (0.0768-
554 0.147) µm^2). As expected, we obtained positive correlations between the mean pixel
555 intensity per AZ measured with confocal and the localization density per AZ measured
556 with localization microscopy (Figure 5E, $r = 0.471$, $p < 0.001$). In addition, the
557 localisation density correlated stronger to the confocally-measured than to the
558 *d*STORM-measured AZ area (Figure 5F, $r = 0.361$, $p < 0.001$ and $r = 0.148$, $p =$
559 0.00618). This indicates that a higher localization density in *d*STORM may lead to an
560 apparent enlargement of AZ area in confocal microscopy and supports the findings of
561 our data simulation.
562
563 **AZ ultrastructure of type Is boutons remains unchanged during acute**
564 **homeostatic plasticity**
565 Finally, we wanted to test whether homeostatic plasticity changes AZs of type Is
566 boutons. Previous work at the *Drosophila* NMJ showed that chronic homeostasis
567 occurs exclusively at type Ib boutons (Newman et al., 2017; Li et al., 2018). However,
568 acute homeostasis has not been imaged so far. Thus, we applied our cluster algorithm
569 to analyze AZs of type Is boutons to clarify potential changes after induction of acute
570 homeostasis (Figure 6A). Remarkably, AZ area, Brp localization numbers and Brp
571 density remained unchanged following PhTx treatment (Figure 6B-D). In addition,
572 subcluster analysis as performed before revealed that PhTx treatment did not change
573 the nanoarrangement of Brp within subclusters during acute homeostasis (Figure 6E-
574 H). We conclude that the restriction of presynaptic plasticity to Ib neuron terminals in
575 chronic homeostasis also holds true for structural rearrangements at the AZ for PhTx
576 induced acute homeostasis.

DISCUSSION

Our localization microscopy data show that the molecular AZ scaffold is compacted at stronger high release probability synapses and rearranged during an acute homeostatic challenge. Brp subclusters are rapidly reorganized during strengthening. PhTx induces changes only at AZs of larger, phasic type Ib boutons, which favors the hypothesis that functional homeostatic plasticity at the *Drosophila* NMJ exclusively demands participation of individual motor inputs. The molecular configuration of AZs including its release sites reflects a certain physiological AZ state and the adaptation to functional demands (Kittel and Heckmann, 2016; Ghelani and Sigrist, 2018). This study introduces a new AZ state characterized by Brp compaction associated with strong synapses, high release probability and during acute homeostatic plasticity.

Distinct molecular architecture and homeostatic response between AZs of low and high release probability

The amount of Brp appears to scale with release probability (Kittel et al., 2006; Peled et al., 2014; Akbergenova et al., 2018). Our study suggests a direct link between the molecular AZ arrangement and its transmission properties. Using localization microscopy and HDBSCAN we show that AZs of phasic type Is boutons are smaller and have higher Brp concentrations than tonic type Ib boutons. Furthermore, our study confirms that Brp is distributed heterogeneously within the AZ and provides evidence that subcluster organization differs substantially between the motor inputs. At high release probability type Is boutons, subclustes are smaller, contain higher Brp concentrations and are located closer to the AZ center. We hypothesize that this compacted nanoarchitecture reflects a high release probability AZ state for positioning of synaptic vesicles closer to release sites.

Differences between homeostatic responses of type Ib and type Is boutons have been described in a model of chronic homeostasis (Newman et al., 2017; Li et al., 2018). We investigated the effects of acute homeostasis and found that structural rearrangements exclusively take place at type Ib AZs (Figures 3 and 6). This either favors the hypothesis that acute homeostatic plasticity is accomplished by distinct molecular mechanisms or, in line with the aforementioned findings, is restricted to type Ib terminals. Wentzel et al., 2018 demonstrated that synaptic vesicles recruited from vesicle pools during acute homeostatic plasticity are highly sensitive to EGTA. Differences in coupling distance between the two motor inputs are conceivable, since

type Is boutons exhibit higher release probabilities and less short-term facilitation. Hence, reduction of the distance between Brp subclusters and the AZ center (containing the highest density of presynaptic voltage-gated calcium channels, VGCCs) in type Is boutons would not lead to further increase in synaptic release. In contrast, more loosely coupled type Ib boutons could profit from further approximation of Brp to VGCCs, observed in localization microscopy as a decrease in radial distance (Figure 3J, Supplementary Figure 5C). Previous work showed a proximo-distal gradient in release probability along type Ib bouton chains (Peled and Isacoff, 2011). To investigate whether this gradient influences the ability of an AZ to undergo homeostatic plasticity, we analyzed the effect of PhTx in type Ib boutons along the string (Paul et al., 2015). Interestingly, PhTx increased Brp density regardless of the bouton position (Figure 3E) indicating that release probability variation along the bouton string is not limiting for AZ compaction during homeostasis.

Compaction of the AZ scaffold without recruitment of Brp molecules

Confocal microscopy revealed an increase in Brp area and intensity after PhTx treatment, interpreted as more Brp molecules (Weyhersmüller et al., 2011; Goel et al., 2017). However, our localization microscopy data provide no evidence for Brp recruitment to the AZ. We suggest that PhTx stimulation leads to an increased Brp density in the AZ and within its subclusters (Figure 3, Supplementary Figure 4). We suggest that AZ compaction is a plasticity pattern to enhance synaptic function and that the increased Brp intensity in confocal microscopy corresponds to the increased protein density due to compaction of the AZ scaffold (Figures 4 and 5). To our knowledge there are no correlative data between confocal microscopy and localization microscopy of AZs available so far. We performed correlative confocal-*d*STORM microscopy and provide evidence that a higher protein density in *d*STORM translates into an apparent area increase in confocal (Figure 5F). Analysis of confocal data was performed using a conventional thresholding approach (Schmid et al., 2008; Weyhersmüller et al., 2011; Goel et al., 2017). This quantification of the spatial extent of fluorescence signal depends on its intensity. Large structures with low intensity can appear smaller than smaller structures with higher intensity (Figures 4D, E and 5C, F). In contrast, in localization microscopy the photon count of the integrated single-molecule signal is used as selection criterion independent of the pixel size of the reconstructed image (Heilemann et al., 2008). Every fluorophore with an intensity over the threshold is treated equally. To emphasize this technical strength, in this study we

left pixel-based quantification and established algorithms working only with the localization coordinates. In combination with HDBSCAN tuned to find stable clusters in data with varying density, we propose an optimized method for analysis of the spatial extent of fluorescence signal. The first super-resolution data on the effects of homeostatic plasticity using STED microscopy reported an increased AZ area in GluRIIA mutants (Weyhersmüller et al., 2011). Our data reveal a more compact Brp scaffold in response to PhTx stimulation. Simulations and correlative confocal-*d*STORM microscopy show that Brp compaction results in an apparent increase of AZ size and numbers of Brp modules as described by Böhme et al., 2019. Furthermore, protein density might also have an impact on the differential regulation of calcium channels at single AZs (Gratz et al., 2019). In addition, it appears that chronic and acute homeostasis display different AZ states with respect to structural adaptation aiming at stabilization of neurotransmission. To this end, chronical challenging of the release machinery can plausibly lead to AZ growth, whereas stabilization during minutes may happen by compaction of already available molecules without protein translation (Frank et al., 2006).

Preceding studies suggested that the AZ scaffold dynamically changes on the minute timescale (Holderith et al., 2012). Different changes are conceivable, (i) decrease in protein numbers and/or AZ size, (ii) increase in protein numbers and/or AZ size or (iii) rearrangement of proteins and/or changes in AZ size. Our data strongly support the third option, which may also be the fastest and most cost-efficient option. Members of the ELKS/CAST family have been shown to regulate the abundance of presynaptic VGCCs and release probability at the Calyx of Held (Dong et al., 2018) and the abundance of RIM and Bassoon was found to scale with the strength of evoked release and AZ area in hippocampal neurons (Matz et al., 2010; Holderith et al., 2012). In *Drosophila* Brp is a well conceivable candidate to change dynamically during homeostatic plasticity (Held and Kaeser, 2018). Our localization microscopy data are in line with these data and suggest a structural correlate of functional homeostasis within presynaptic terminals.

AZ nanoscopy

Localization microscopy provides information about how AZs change during presynaptic plasticity (Tang et al., 2016; Glebov et al., 2017) and allows to decipher

how amount and arrangement of certain presynaptic proteins are adapted (Nusser, 2018). RIM clusters with diameters of ~80 nm were described in hippocampal neurons and show remarkable reorganization during synaptic plasticity (Tang et al., 2016). We believe that at the *Drosophila* AZ Brp subclusters are important functional units likewise. Considering the size of an individual subcluster (1.6 x 10^{-3} µm^2, Figure 2D, 3G) corresponding to a circle with ~50 nm diameter, *d*STORM localization precision is not limiting (Supplementary Figure 1). However, due to the size of the primary-secondary antibody complex estimated to be around 13 nm (Ehmann et al., 2014), which gives a minimum diameter of 26 nm, subcluster size could still be overestimated and Brp density could be even higher. Böhme et al., 2019 using STED microscopy found fewer Brp subclusters per AZ compared to Ehmann et al., 2014 and the present study. We assume that these differences are caused by different imaging and data evaluation approaches. The drawbacks of a thresholding-based analysis illustrated for confocal microscopy are also evident for quantification of STED data. However, it is possible that STED data describe an intermediate of 6-7 subclusters containing the 15 subclusters revealed by *d*STORM. A related issue is the apparent ring like arrangement of Brp in STED images of AZs (Kittel et al., 2006; Weyhersmüller et al., 2011; Böhme et al., 2019). In our *d*STORM measurements of Brp in AZs rings are less prominent which is probably due to resolution (more prominent rings appearing at the center of the images in Fig. 4F). In addition, only a fraction of AZs has a circular shape (Supplementary Figure 5A), thus, the ring configuration is not a property of all AZs.

As the structure of *Drosophila* AZs is highly diverse (Figures 1C and 3B) we aimed for an unbiased way of data selection to prevent subjective bias and to represent the heterogeneous population with respect to projection artifacts and orientation (Pauli et al., 2019). Furthermore, the here presented algorithm allowed fast and automated analysis of the whole data set or of a subsample of AZs (Supplementary Figure 5). The density-based clustering approach detects clusters in data with varying density. Nevertheless, it's unclear if clustering of other AZ molecules coincides with functional synaptic properties. In the mammalian cerebellum tightly coupled stellate synapses exhibit clustering of VGCCs, whereas loosely coupled granule cell synapses show a non-clustered VGCC distribution (Rebola et al., 2019).

Our HDBSCAN-based analysis detected fewer subclusters in high release probability type Is AZs. Considering the increased localization density, we cannot rule out that changes in subcluster numbers depend on signal density. Localization density in phtx was increased to a similar extent without change in absolute subcluster numbers, which shows in principle that changes in subcluster numbers can be independent. The formation of synaptic vesicle clusters depends on liquid-liquid phase separation, that is achieved by intrinsically disordered regions (IDRs) that do not fold into any stable secondary or tertiary structures (Milovanovic et al., 2018). Glutamine-rich IDRs have also been implicated in the formation of coiled-coils and protein agglomerates (Fiumara et al., 2010). In liquid-liquid phase separations of prion-like FUS (Fused in Sarcoma) family proteins, tyrosine and arginine residues govern the saturation concentration of phase separation, glycine residues maintain liquidity, wheras glutamine and serine residues promote hardening (Wang et al., 2018). The C-terminal end of Brp tethers synaptic vesicles and comprises a stretch of glutamine residues (Hallermann et al., 2010). AZ compaction during homeostasis could arise from vesicles engaging in liquid-liquid phase separation with Brp C-terms. While the molecular binding partners of the Brp C-term are still unclear, a functional interaction with Complexin was reported (Scholz et al., 2019). Regarding the aforementioned model of phase separation of vesicles and Brp and the position of the Brp^{Nc82} epitope, it is also attractive to speculate that all Brp molecules forming one subcluster might tether a single synaptic vesicle. This hypothesis matches with EM studies describing on average 12 vesicles tethered to a single CAZ (Böhme et al., 2016) and with reconstructions of EM tomography data (Zhan et al., 2016). Finally, it appears promising to correlate the transmission properties of an individual AZ using transgenically expressed GCaMP Ca^{2+} sensors (Akbergenova et al., 2018; Gratz et al., 2019) with its nanoarchitecture imaged with super-resolution microscopy to link synaptic activity with ultrastructure.

AUTHOR CONTRIBUTIONS

A.M., J.E., A.L.S., M.S., M.H. and M.M.P designed experiments. A.M., M.P., M.H. and M.M.P. performed experiments. A.M., P.K., F.R., M.P., R.J.K., J.E., S.D., M.H. and M.M.P analyzed the data. A.M., M.H. and M.M.P. wrote the manuscript with the help of all co-authors. A.L.S., M.S., M.H. and M.M.P. coordinated the study and provided funding.

ACKNOWLEDGEMENTS

This work was supported by grants from the German Research Foundation (DFG) TRR166/B06 to A.L.S. and M.H., TRR166/B02 to S.D., TRR166/B04 to M.S., KI1460/5-1 and KI1460/4-1 to R.J.K. and from the IZKF Würzburg to A.L.S. and M.H. (N229). The authors thank T. Langenhan for scientific discussions and M. Oppmann and F. Köhler for excellent technical assistance. The authors declare no conflict of interest.

REFERENCES

Akbergenova Y, Cunningham KL, Zhang YV, Weiss S, Littleton JT. 2018. Characterization of developmental and molecular factors underlying release heterogeneity at Drosophila synapses. *Elife* **10**:7. doi: 10.7554/eLife.38268.

Atwood HL, Govind CK, Wu CF. 1993. Differential ultrastructure of synaptic terminals on ventral longitudinal abdominal muscles in Drosophila larvae. *Journal of Neurobiology* **24**:1008-1024.

Atwood HL, Karunanithi S. 2002. Diversification of synaptic strength: presynaptic elements. *Nature Reviews Neuroscience* **3**:497-516.

Bar-On D, Wolter S, van de Linde S, Heilemann M, Nudelmann G, Nachliel E, Gutman M, Sauer M, Ashery U. 2012. Super-resoluation imaging reveals the internal architecture of nanosized syntaxin clusters. *Journal of Biological Chemistry* **287**:27158-27167 doi: 10.1074/jbc.M112.353250.

Böhme MA, Beis C, Reddy-Alla S, Reynolds E, Mampell MM, Grasskamp AT, Lützkendorf J, Bergeron DD, Driller JH, Babikir H, Göttfert F, Robinson IM, O'Kane CJ, Hell SW, Wahl MC, Stelzl U, Loll B, Walter AM, Sigrist SJ. 2016. Active zone scaffolds differentially accumulate Unc13 isoforms to tune Ca^{2+} channel-vesicle coupling. *Nature Neuroscience* **19**:1311-1320. doi: 10.1038/nn.4364.

Böhme MA, McCarthy AW, Grasskamp AT, Beuschel CB, Goel P, Jusyte M, Laber D, Huang S, Rey U, Petzoldt AG, Lehmann M, Göttfert F, Haghighi P, Hell SW, Owald D, Dickman D, Sigrist SJ, Walter AM. 2019. Rapid active zone remodeling consolidates presynaptic potentiation. *Nature Communications* **10**:1085. doi: 10.1038/s41467-019-08977-6.

Campello RJ, Moulavi D, Sander J. 2013. Density-based clustering based on hierarchical density estimates. *In Pacific-Asia Conference on Knowledge Discovery and Data Mining*. pp. 160-172. Springer Berlin Heidelberg.

Davis GW, Müller M. 2015. Homeostatic control of presynaptic neurotransmitter release. *Annual Review of Physiology* **77**:251-270. doi: 10.1146/annurev-physiol-021014-071740.

Dittman JS, Kreitzer AC, Regehr WG. 2000. Interplay between facilitation, depression, and residual calcium at three presynaptic terminals. *Journal of Neuroscience* **20**:1374-1385.

Dong W, Radulovic T, Goral RO, Thomas C, Suarez Montesinos M, Guerrero-Given D, Hagiwara A, Putzke T, Hida Y, Abe M, Sakimura K, Kamasawa N, Ohtsuka T, Young SM Jr. 2018. CAST/ELKS Proteins Control Voltage-Gated Ca^{2+} Channel Density and Synaptic Release Probability at a Mammalian Central Synapse. *Cell Reports* **24**:284-293. doi: 10.1016/j.celrep.2018.06.024.

Edelsbrunner H, Mücke EP. 1994. Three-dimensional alpha shapes. *ACM Transactions on Graphics* **13**:43–72. doi: 10.1145/174462.156635.

Ehmann N, van de Linde S, Alon A, Ljaschenko D, Keung XZ, Holm T, Rings A, DiAntonio A, Hallermann S, Ashery U, Heckmann M, Sauer M, Kittel RJ. 2014. Quantitative super-resolution imaging of Bruchpilot distinguishes active zone states. *Nature Communications* **5**:4650. doi: 10.1038/ncomms5650.

Endesfelder U, Malkusch S, Fricke F, Heilemann M. 2014. A simple method to estimate the average localization precision of a single-molecule localization microscopy experiment. *Histochemistry and Cell Biology* **141**:629-38. doi: 10.1007/s00418-014-1192-3.

Ester M, Kriegel HP, Sander J, Xu X. 1996. A Density-Based Algorithm for Discovering Clusters in Large Spatial Databases with Noise. *Proc. 2nd Int. Conf. on Knowledge Discovery and Data Mining*. Portland OR:226-231.

Fiumara F, Fioriti L, Kandel ER, Hendrickson WA. 2010. Essential role of coiled coils for aggregation and activity of Q/N-rich prions and PolyQ proteins. *Cell* **143**:1121-35. doi: 10.1016/j.cell.2010.11.042.

Fouquet W, Owald D, Wichmann C, Mertel S, Depner H, Dyba M, Hallermann S, Kittel RJ, Eimer S, Sigrist SJ. 2009. Maturation of active zone assembly by Drosophila Bruchpilot. *Journal of Cell Biology* **186**:129-145. doi: 10.1083/jcb.200812150.

Frank CA, Kennedy MJ, Goold CP, Marek KW, Davis GW. 2006. Mechanisms underlying the rapid induction and sustained expression of synaptic homeostasis. *Neuron* **52**:663-677.

Ghelani T, Sigrist SJ. 2018. Coupling the Structural and Functional Assembly of Synaptic Release Sites. *Frontiers in Neuroanatomy* **12**:81. doi: 10.3389/fnana.2018.00081.

Glebov OO, Jackson RE, Winterflood CM, Owen DM, Barker EA, Doherty P, Ewers H, Burrone J. 2017. Nanoscale Structural Plasticity of the Active Zone Matrix Modulates Presynaptic Function. *Cell Reports* **18**:2715-2728. doi: 10.1016/j.celrep. 2017.02.064.

Goel P, Li X, Dickman D. 2017. Disparate Postsynaptic Induction Mechanisms Ultimately Converge to Drive the Retrograde Enhancement of Presynaptic Efficacy. *Cell Reports* **21**:2339-2347. doi: 10.1016/j.celrep.2017.10.116.

Gratz SJ, Goel P, Bruckner JJ, Hernandez RX, Khateeb K, Macleod GT, Dickman D, O'Connor-Giles KM. 2019. Endogenous Tagging Reveals Differential Regulation of Ca^{2+} Channels at Single Active Zones during Presynaptic Homeostatic Potentiation and Depression. *Journal of Neuroscience* **39**:2416-2429. doi: 10.1523/JNEUROSCI.3068-18.2019.

Hallermann S, Kittel RJ, Wichmann C, Weyhersmüller A, Fouquet W, Mertel S, Owald D, Eimer S, Depner H, Schwärzel M, Sigrist SJ, Heckmann M. 2010. Naked dense bodies provoke depression. *Journal of Neuroscience* **30**:14340-14345. doi: 10.1523/JNEUROSCI.2495-10.2010.

Heilemann M, van de Linde S, Schüttpelz M, Kasper R, Seefeldt B, Mukherjee A, Tinnefeld P, Sauer M. 2008. Subdiffraction-Resolution Fluorescence Imaging with

Conventional Fluorescent Probes. *Angewandte Chemie International Edition* **33**:6172-6176. doi: 10.1002/anie.200802376.

Held RG, Liu C, Kaeser PS. 2016. ELKS controls the pool of readily releasable vesicles at excitatory synapses through its N-terminal coiled-coil domains. *Elife* **5**:e14862. doi: 10.7554/eLife.14862.

Held RG, Kaeser PS. 2018. ELKS active zone proteins as multitasking scaffolds for secretion. *Open Biology* **8**:170258. doi: 10.1098/rsob.170258.

Hoang B, Chiba A. 2001. Single-cell analysis of Drosophila larval neuromuscular synapses. *Developmental Biology* **229**:55-70.

Holderith N, Lorincz A, Katona G, Rózsa B, Kulik A, Watanabe M, Nusser Z. 2012. Release probability of hippocampal glutamatergic terminals scales with the size of the active zone. *Nature Neuroscience* **15**:988-997. doi: 10.1038/nn.3137.

Karunanithi S, Marin L, Wong K, Atwood HL. 2002. Quantal size and variation determined by vesicle size in normal and mutant Drosophila glutamatergic synapses. *Journal of Neuroscience* **22**:10267-10276.

Kiskowski MA, Hancock JF, Kenworthy AK. 2009. On the use of Ripley's K-function and its derivatives to analyze domain size. *Biophysical Journal* **97**:1095-103. doi: 10.1016/j.bpj.2009.05.039.

Kittel RJ, Wichmann C, Rasse TM, Fouquet W, Schmidt M, Schmid A, Wagh DA, Pawlu C, Kellner RR, Willig KI, Hell SW, Buchner E, Heckmann M, Sigrist SJ. 2006. Bruchpilot promotes active zone assembly, Ca^{2+} channel clustering, and vesicle release. *Science* **312**:1051-1054.

Kittel RJ, Heckmann M. 2016. Synaptic Vesicle Proteins and Active Zone Plasticity. *Frontiers in Synaptic Neuroscience* **8**:8. doi: 10.3389/fnsyn.2016.00008.

Kurdyak P, Atwood HL, Stewart BA, Wu CF. 1994. Differential physiology and morphology of motor axons to ventral longitudinal muscles in larval Drosophila. *Journal of Comparative Neurology* ***350***:463-472.

Li X, Goel P, Wondolowski J, Paluch J, Dickman D. 2018. A Glutamate Homeostat Controls the Presynaptic Inhibition of Neurotransmitter Release. *Cell Reports* **23**:1716-1727. doi: 10.1016/j.celrep.2018.03.130.

Liu KS, Siebert M, Mertel S, Knoche E, Wegener S, Wichmann C, Matkovic T, Muhammad K, Depner H, Mettke C, Bückers J, Hell SW, Müller M, Davis GW, Schmitz D, Sigrist SJ. 2011. RIM-binding protein, a central part of the active zone, is essential for neurotransmitter release. *Science* **334**:1565-1569. doi: 10.1126/science.1212991.

Lnenicka GA, Keshishian H. 2000. Identified motor terminals in Drosophila larvae show distinct differences in morphology and physiology. *Journal of Neurobiology* **43**:186-197.

Löschberger A, van de Linde S, Dabauvalle MC, Rieger B, Heilemann M, Krohne G,

Sauer M. 2012. Super-resolution imaging visualizes the eightfold symmetry of gp210 proteins around the nuclear pore complex and resolves the central channel with nanometer resolution. *Journal of Cell Science* **125**:570-575. doi: 10.1242/jcs.098822.

Lu Z, Chouhan AK, Borycz JA, Lu Z, Rossano AJ, Brain KL, Zhou Y, Meinertzhagen IA, Macleod GT. 2016. High-Probability Neurotransmitter Release Sites Represent an Energy-Efficient Design. *Current Biol*ogy **26**:2562-2571. doi: 10.1016/j.cub.2016.07.032.

Malkusch S, Heilemann M. 2016. Extracting quantitative information from single-molecule super-resolution imaging data with LAMA - LocAlization Microscopy Analyzer. *Science Reports* **6**:34486. doi: 10.1038/srep34486.

Matz J, Gilyan A, Kolar A, McCarvill T, Krueger SR. 2010. Rapid structural alterations of the active zone lead to sustained changes in neurotransmitter release. *Proceedings of the National Academy of Sciences* **107**:8836-8841. doi: 10.1073/pnas.0906087107.

McInnes L, Healy J, Astels S. 2017. hdbscan: Hierarchical density based clustering, *Journal of Open Source Software* **2**:205. doi:10.21105/joss.00205.

Milovanovic D, Wu Y, Bian X, De Camilli P. 2018. A liquid phase of synapsin and lipid vesicles. *Science* **361**:604-607. doi: 10.1126/science.aat5671.

Neher E, Brose N. 2018. Dynamically Primed Synaptic Vesicle States: Key to Understand Synaptic Short-Term Plasticity. *Neuron* **100**:1283-1291. doi: 10.1016/j.neuron.2018.11.024.

Newman ZL, Hoagland A, Aghi K, Worden K, Levy SL, Lee LP, Isacoff EY. 2017. Input-Specific Plasticity and Homeostasis at the Drosophila Larval Neuromuscular Junction. *Neuron* **93**:1388-1404. doi: 10.1016/j.neuron.2017.02.028.

Nusser Z. 2018. Creating diverse synapses from the same molecules. *Current Opinion in Neurobiology* **51**:8-15. doi: 10.1016/j.conb.2018.01.001.

Palay SL, Chan-Palay V. 1974. Cerebellar Cortex – Cytology and Organization. *Springer Verlag Berlin Heidelberg*.

Paul MM, Pauli M, Ehmann N, Hallermann S, Sauer M, Kittel RJ, Heckmann M. 2015. Bruchpilot and Synaptotagmin collaborate to drive rapid glutamate release and active zone differentiation. *Frontiers in Cellular Neuroscience* **9**:29. doi: 10.3389/fncel.2015.00029.

Pauli M, Paul MM, Proppert S, Sharifi M, Repp F, Kollmannsberger P, Sauer M, Heckmann M, Sirén AL. 2019. Targeted volumetric single-molecule localization microscopy of defined presynaptic structures in brain sections. *bioRxiv* March 05, 2019. doi: https://doi.org/10.1101/568279.

Pedregosa F, Varoquaux G, Gramfort A, Michel V, Thirion B, Grisel O, Blondel M, Prettenhofer P, Weiss R, Dubourg V, Vanderplas J, Passos A, Cournapeau D, Brucher M, Perrot M, Duchesnay E. 2011. Scikit-learn: Machine Learning in Python. *Journal of Machine Learning Research* **12**:2825−2830.

965 Peled ES, Newman ZL, Isacoff EY. 2014. Evoked and spontaneous transmission
966 favored by distinct sets of synapses. *Current Biology* **24**:484-493. doi:
967 10.1016/j.cub.2014.01.022.
968
969 Peled ES, Isacoff EY. 2011. Optical quantal analysis of synaptic transmission in wild-
970 type and rab3-mutant Drosophila motor axons. *Nature Neuroscience* **14**:519-526. doi:
971 10.1038/nn.2767.
972
973 Rebola N, Reva M, Kirizs T, Szoboszlay M, Lőrincz A, Moneron G, Nusser Z,
974 DiGregorio DA. 2019. Distinct Nanoscale Calcium Channel and Synaptic Vesicle
975 Topographies Contribute to the Diversity of Synaptic Function. *Neuron* doi:
976 10.1016/j.neuron.2019.08.014. [Epub ahead of print]
977
978 Robitaille TP, Tollerud EJ, Greenfield P, Droettboom M, Bray E, Aldcroft T, Davis M,
979 Ginsburg A, Price-Whelan AM, Kerzendorf WE, Conley A, Crighton N, Barbary K,
980 Muna D, Ferguson H, Grollier F, Parikh MM, Nair PH, Günther HM, Deil C, Woillez J,
981 Conseil S, Kramer R, Turner JEH, Singer L, Fox R, Weaver BA, Zabalza V, Edwards
982 ZI, Bostroem KA, Burke DJ, Casey AR, Crawford SM, Dencheva N, Ely J, Jenness T,
983 Labrie K, Lim PL, Pierfederici F, Pontzen A, Ptak A, Refsdal B, Servillat M, Streicher
984 O. 2013. Astropy: A community Python package for astronomy. *Astronomy &*
985 *Astrophysics* **558**:A33. doi: 10.1051/0004-6361/201322068.
986
987 Schindelin J, Arganda-Carreras I, Frise E, Kaynig V, Longair M, Pietzsch T, Preibisch
988 S, Rueden C, Saalfeld S, Schmid B, Tinevez JY, White DJ, Hartenstein V, Eliceiri K,
989 Tomancak P, Cardona A. 2012. Fiji: an open-source platform for biological-image
990 analysis. *Nature methods* **7**:676-682. doi:10.1038/nmeth.2019.
991
992 Schmid A, Hallermann S, Kittel RJ, Khorramshahi O, Frölich AM, Quentin C, Rasse
993 TM, Mertel S, Heckmann M, Sigrist SJ. 2008. Activity-dependent site-specific changes
994 of glutamate receptor composition in vivo. *Nature Neuroscience* **11**:659-66. doi:
995 10.1038/nn.2122. Epub 2008 May 11.
996
997 Schmidt H, Brachtendorf S, Arendt O, Hallermann S, Ishiyama S, Bornschein G, Gall
998 D, Schiffmann SN, Heckmann M, Eilers J. 2013. Nanodomain coupling at an excitatory
999 cortical synapse. *Current Biology* **23**:244-249. doi: 10.1016/j.cub.2012.12.007.
1000
1001 Scholz N, Ehmann N, Sachidanandan D, Imig C, Cooper BJ, Jahn O, Reim K, Brose
1002 N, Meyer J, Lamberty M, Altrichter S, Bormann A, Hallermann S, Pauli M, Heckmann
1003 M, Stigloher C, Langenhan T, Kittel RJ. 2019. Complexin cooperates with Bruchpilot
1004 to tether synaptic vesicles to the active zone cytomatrix. *Journal of Cell Biology*
1005 **218**:1011-1026. doi: 10.1083/jcb.201806155. Epub 2019 Feb 19.
1006
1007 Stewart BA, Atwood HL, Renger JJ, Wang J, Wu CF. 1994. Improved stability of
1008 Drosophila larval neuromuscular preparations in haemolymph-like physiological
1009 solutions. *Journal of Comparative Physiology* **175**:179-191.
1010
1011 Südhof TC. 2012. The presynaptic active zone. *Neuron* **75**:11-25. doi:
1012 10.1016/j.neuron.2012.06.012.
1013
1014 Szoboszlay M, Kirizs T, Nusser Z. 2017. Objective quantification of nanoscale protein
1015 distributions. *Science Reports* **7**:15240. doi: 10.1038/s41598-017-15695-w.

Tang AH, Chen H, Li TP, Metzbower SR, MacGillavry HD, Blanpied TA. 2016. A trans-synaptic nanocolumn aligns neurotransmitter release to receptors. *Nature* **536:**210-4.

Taschenberger H, Leão RM, Rowland KC, Spirou GA, von Gersdorff H. 2002. Optimizing synaptic architecture and efficiency for high-frequency transmission. *Neuron* **36**:1127-1143.

Valera AM, Doussau F, Poulain B, Barbour B, Isope P. 2012. Adaptation of granule cell to Purkinje cell synapses to high-frequency transmission. *Journal of Neuroscience* **32**:3267-3280. doi: 10.1523/JNEUROSCI.3175-11.2012.

van de Linde S, Sauer M, Heilemann M. 2008. Subdiffraction-resolution fluorescence imaging of proteins in the mitochondrial inner membrane with photoswitchable fluorophores. *Journal of Structural Biology* **164**:250-254. doi: 10.1016/j.jsb.2008.08.002. Epub 2008 Aug 26.

van de Linde S, Löschberger A, Klein T, Heidbreder M, Wolter S, Heilemann M Sauer M. 2011 Direct stochastic optical reconstruction microscopy with standard fluorescent probes. *Nature Protocols* **7**:991–1009.

Wang J, Choi JM, Holehouse AS, Lee HO, Zhang X, Jahnel M, Maharana S, Lemaitre R, Pozniakovsky A, Drechsel D, Poser I, Pappu RV, Alberti S, Hyman AA. 2018. A Molecular Grammar Governing the Driving Forces for Phase Separation of Prion-like RNA Binding Proteins. *Cell* **174**:688-699.e16. doi: 10.1016/j.cell.2018.06.006.

Wentzel C, Delvendahl I, Sydlik S, Georgiev O, Müller M. 2018. Dysbindin links presynaptic proteasome function to homeostatic recruitment of low release probability vesicles. *Nature Communications* **9**:267. DOI: https://doi.org/ 10.1038/s41467-017-02494-0.

Weyhersmüller A, Hallermann S, Wagner N, Eilers J. 2011. Rapid active zone remodeling during synaptic plasticity. *Journal of Neuroscience* **31**:6041-6052. doi: 10.1523/JNEUROSCI.6698-10.2011.

Wolter S, Schüttpelz M, Tscherepanow M, van de Linde S, Heilemann M, Sauer M. 2010. Real-time computation of subdiffraction-resolution fluorescence images. *Journal of Microscopy* **237**:12-22. doi: 10.1111/j.1365-2818.2009.03287.x.

Wolter S, Löschberger A, Holm T, Aufmkolk S, Dabauvalle MC, van de Linde S, Sauer M. 2012. rapidSTORM: Accurate, fast and open-source software for localization microscopy. *Nature Methods* **9**:1040-1041. doi: 10.1038/nmeth.2224.

Xu-Friedman MA, Harris KM, Regehr WG. 2001. Three-dimensional comparison of ultrastructural characteristics at depressing and facilitating synapses onto cerebellar Purkinje cells. *Journal of Neuroscience* **21**:6666-6672.

Zhan H, Bruckner J, Zhang Z, O'Connor-Giles K. 2016. Three-dimensional imaging of Drosophila motor synapses reveals ultrastructural organizational patterns. *Journal of Neurogenetics* **30**:237-246. DOI: 10.1080/01677063.2016.1253693.

FIGURES

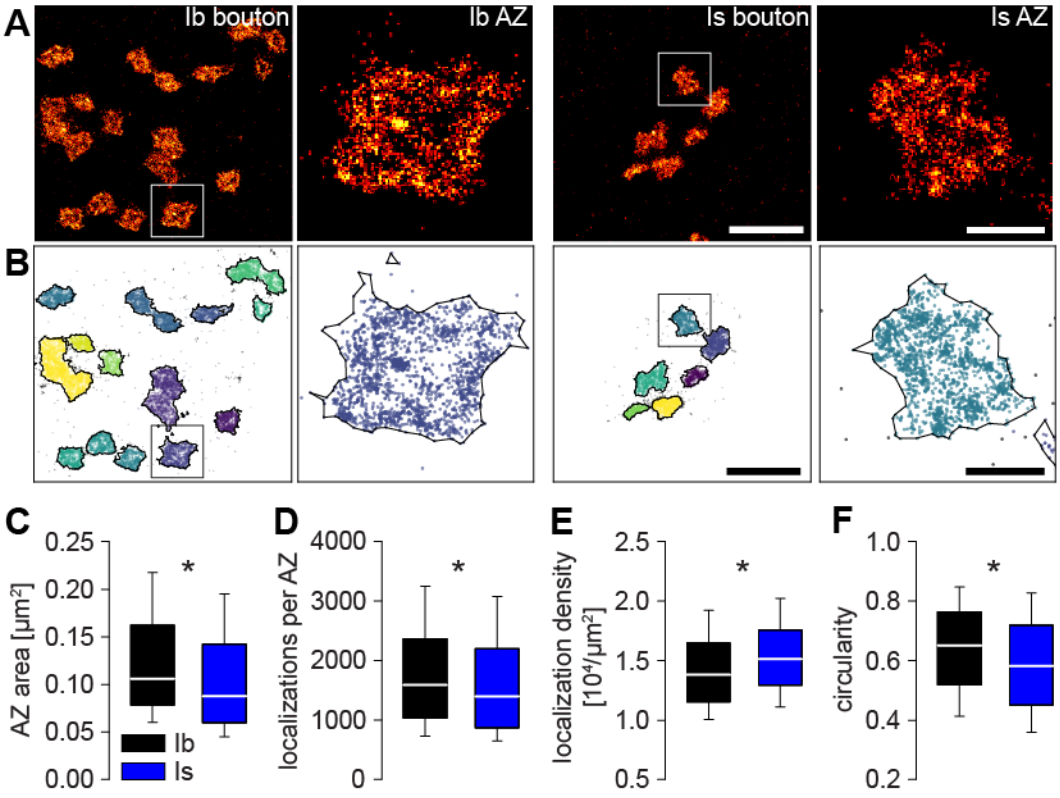

Figure 1. More compact Brp arrangement at AZs of type Is boutons.

(A) Representative *d*STORM images of a type Ib bouton and a type Is bouton of a wildtype *Drosophila* NMJ on abdominal muscles 6/7 stained with Brp^{Nc82} antibody labelled with Alexa Fluor647 conjugated $F(ab')_2$ fragments. Enlargement of boxed AZs. Scale bars in (A, B) 1 µm for boutons and 200 nm for AZs.

(B) Boutons and AZs from (A) displayed via the analysis algorithm used throughout this manuscript. Individual AZs are surrounded by black lines indicating alpha shapes to determine AZ area and circularity, clustered Brp localizations are shown as colored dots (with colors indicating cluster identity), unclustered Brp localizations as grey dots.

(C) AZ area in type Ib boutons (black, for C-F n = 1120 AZs from 22 NMJs from 10 animals) and type Is boutons (blue, for C-F n = 673 AZs from 18 NMJs from 10 animals) shown as box plots.

(D-F) Number of Brp localizations per individual AZ, Brp localization density and AZ circularity in both bouton types.

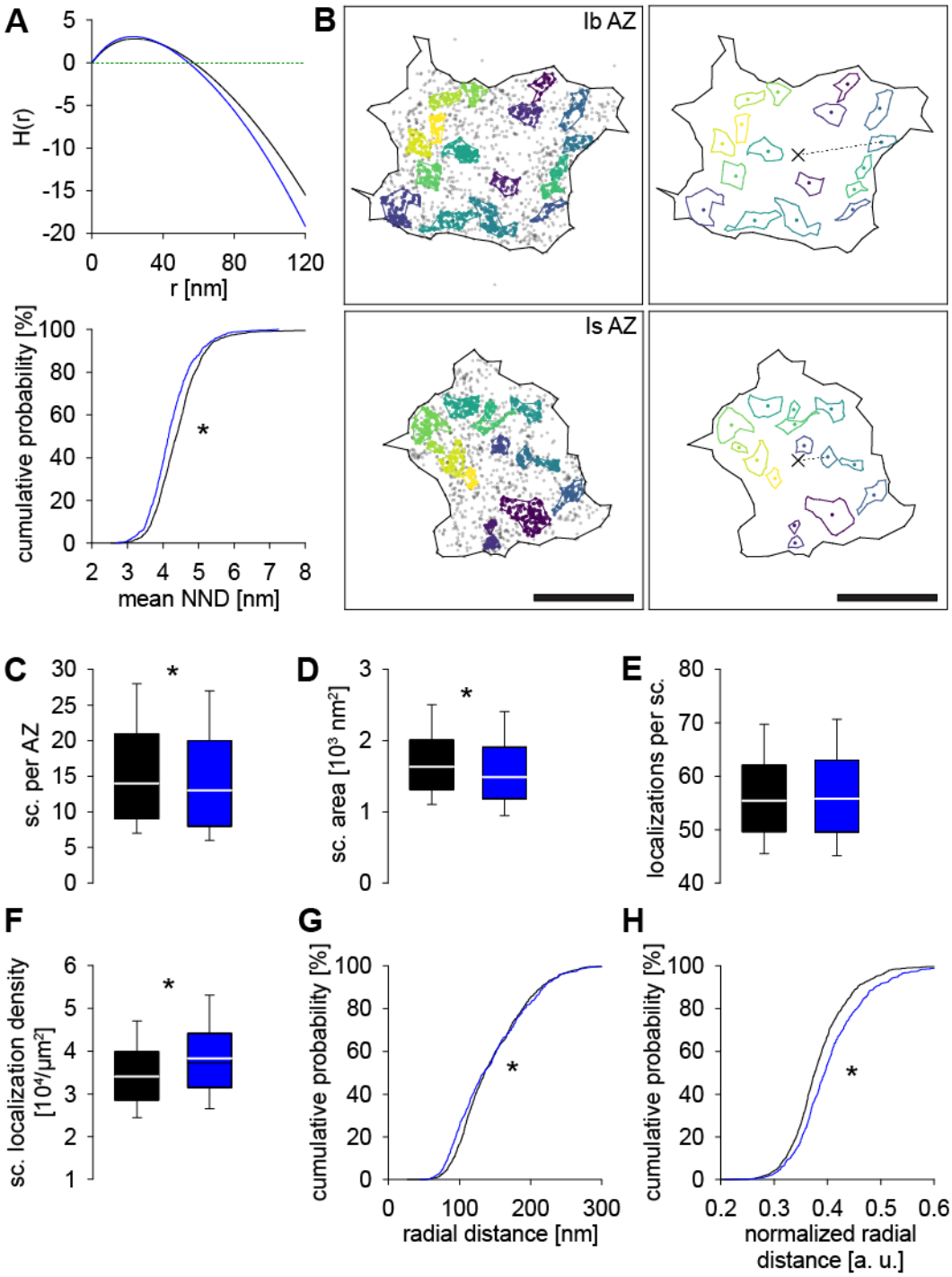

Figure 2. Distinct Brp subcluster organization in type Ib and type Is boutons.

(A) Upper panel: Averaged H functions (derivative from Ripley's K function, see Material and Methods) of all AZs of type Ib (black) and type Is boutons (blue). Lower panel: Cumulative plots of the mean nearest neighbor distance (NND) of all Brp localizations per AZ in type Ib (n = 1120 AZs from 22 NMJs from 10 animals) and type Is boutons (n = 673 AZs from 18 NMJs from 10 animals).

(B) Left panels: Scatter plots illustrating the analysis algorithm applied to AZs shown in Figure 1B with colored Brp subclusters surrounded by colored lines indicating alpha

shapes for area determination. Unclustered Brp localizations are displayed as grey dots. Right panels: Determination of the center of mass (c.o.m.) of the AZ (cross) and of individual subclusters (colored dots) for measurement of radial distances (exemplified by dashed line for one subcluster). Scale bars 200 nm.

(C) Subcluster numbers per individual type Ib AZ (for C-H n = 1120 AZs from 22 NMJs from 10 animals) and type Is AZ (for C-H n = 673 AZs from 18 NMJs from 10 animals).

(D-F) Subcluster area (D), number of Brp localizations per subcluster (E) and Brp localization density (F) in both bouton types.

(G) Cumulative plots of the radial distance between the AZ c.o.m. and the c.o.m. of individual subclusters in both bouton types.

(H) Cumulative plots of radial distances shown in (G) normalized to the AZ area.

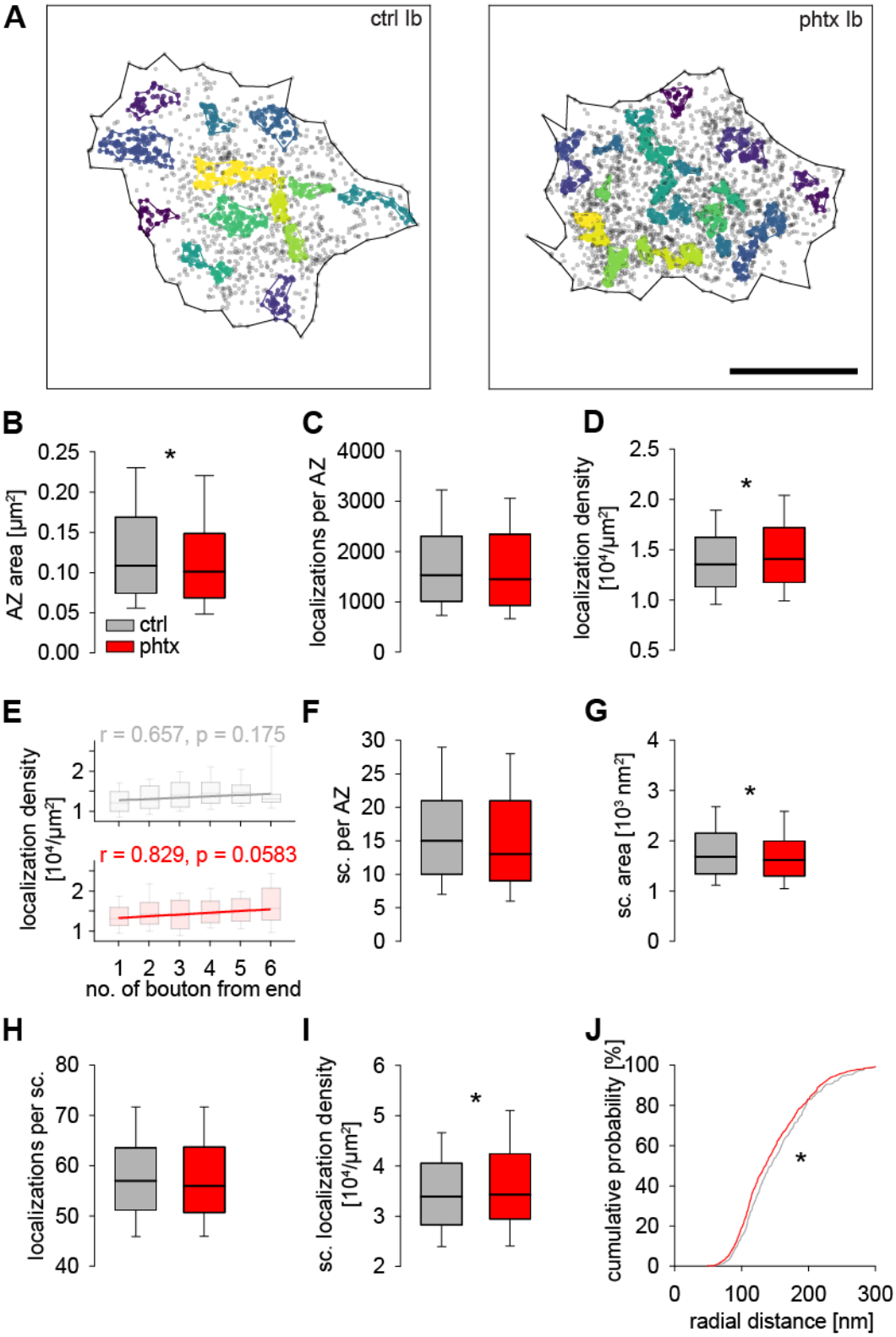

Figure 3. Acute homeostatic plasticity decreases AZ size, enhances Brp localization density and changes subcluster organization in type Ib boutons.

(A) Scatter plots of type Ib AZs from a control animal (ctrl, left) and a Philanthotoxin treated animal (phtx, right), respectively. Scale bar 200 nm.

(B-D) AZ area (B), number of Brp localizations per AZ (C) and Brp localization density (D) in ctrl (grey, for B-J n = 568 AZs from 13 NMJs from 6 animals) and phtx larvae (red, for B-J n = 792 AZs from 14 NMJs from 5 animals).

(E) Brp localization density in both groups shown as boxplots for individual boutons number 1-6 from the end of the bouton string. Spearman correlation coefficients show no significant correlation between AZ localization density and bouton position in ctrl (n = 240, 140, 102, 71, 54, 19 AZs for boutons 1-6) and phtx (n = 251, 134, 146, 117, 78, 51 AZs for boutons 1-6, respectively).

(F-I) Subcluster numbers per type Ib AZ (F), subcluster area (G), the number of Brp localizations per subcluster (H) and Brp localization density (I) in ctrl and phtx.

(J) Cumulative plots of the radial distance between the AZ c.o.m. and the c.o.m. of individual subclusters in both groups.

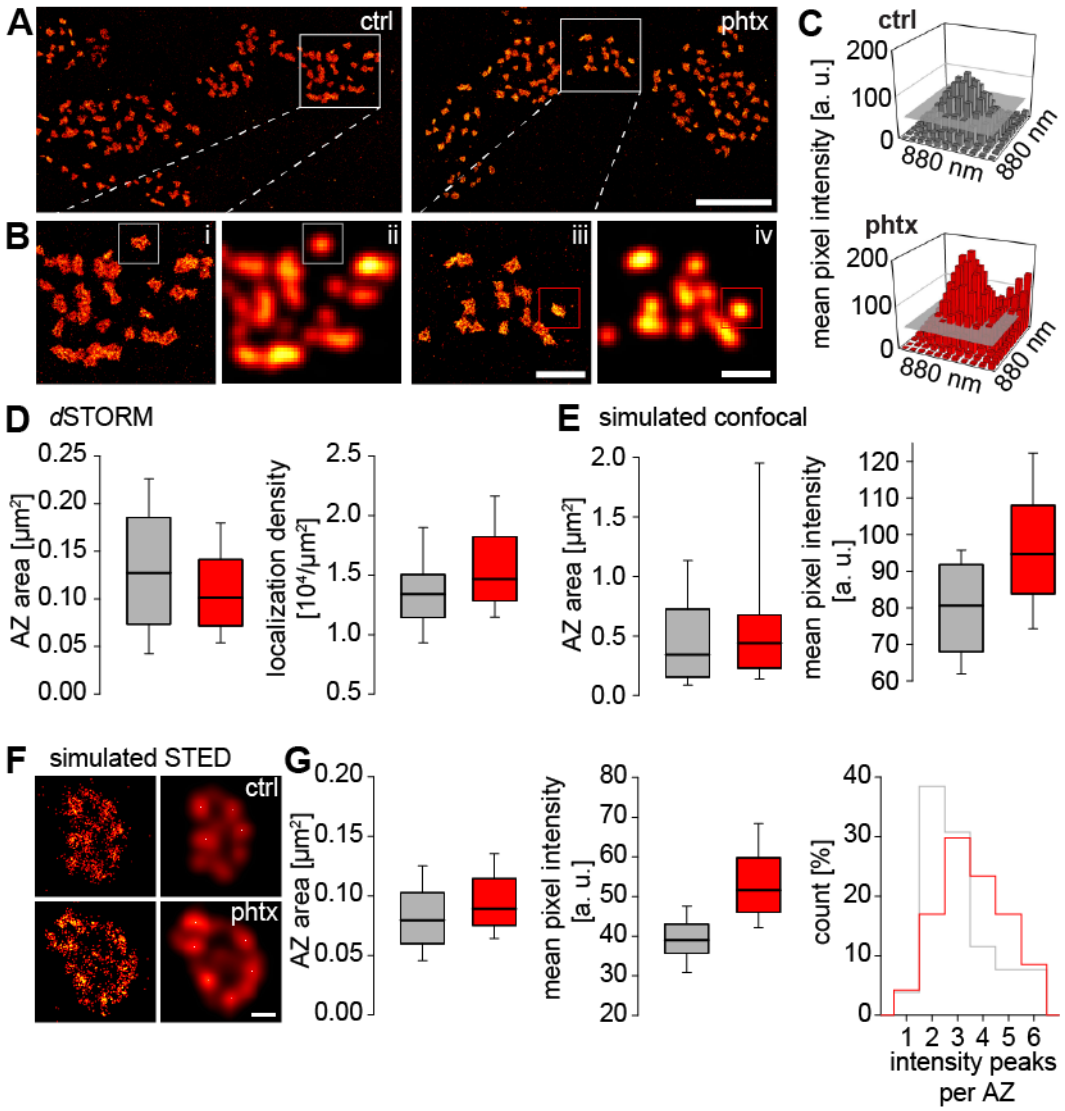

Figure 4. Nanoscale molecular compaction appears as increased area and intensity in confocal simulation and as more Brp clusters in STED simulation.

(A) Sections of *d*STORM images in ctrl and phtx in resolution generally used in this manuscript (5 nm binning, Material and Methods). Boxes highlight enlarged regions in (B). Scale bar 4 µm.

(B) Enlarged regions from (A) with *d*STORM resolution (i / iii) and simulated confocal resolution (ii / iv, 80 nm pixels, 150 nm Gaussian blur). Boxes highlight selected AZs in (C). Scale bars 1.2 µm.

(C) 3D bar plots of mean pixel intensity in confocal resolution of boxed AZs in (B). Grey plane indicates thresholding level of 50 a. u. which was used for quantification in (E).

(D) AZ area and Brp localizations obtained from *d*STORM analysis in ctrl (grey, n = 57 AZs) and phtx (red, n = 100 AZs).

(E) AZ area and mean pixel intensity quantified as shown in (C), i.e. by assuming confocal resolution, in ctrl (n = 30 AZs) and phtx (n = 35 AZs). Note that confluence of

1136 individual Brp spots at this level of resolution leads to a deviant number of AZs
1137 compared to (D).
1138 (F) Example type Ib AZs of ctrl (upper panels) and phtx (lower panels) in *d*STORM
1139 resolution (left) and simulated STED resolution (25 nm Gaussian blur, right). White
1140 spots indicate maxima detected with FIJI peak finding algorithm.
1141 (G) AZ area, mean pixel intensity and number of intensity peaks, i.e. Brp modules, per
1142 AZ obtained from simulated STED analysis (Material and Methods) in ctrl (n = 26 AZs)
1143 and phtx (n = 47 AZs).
1144

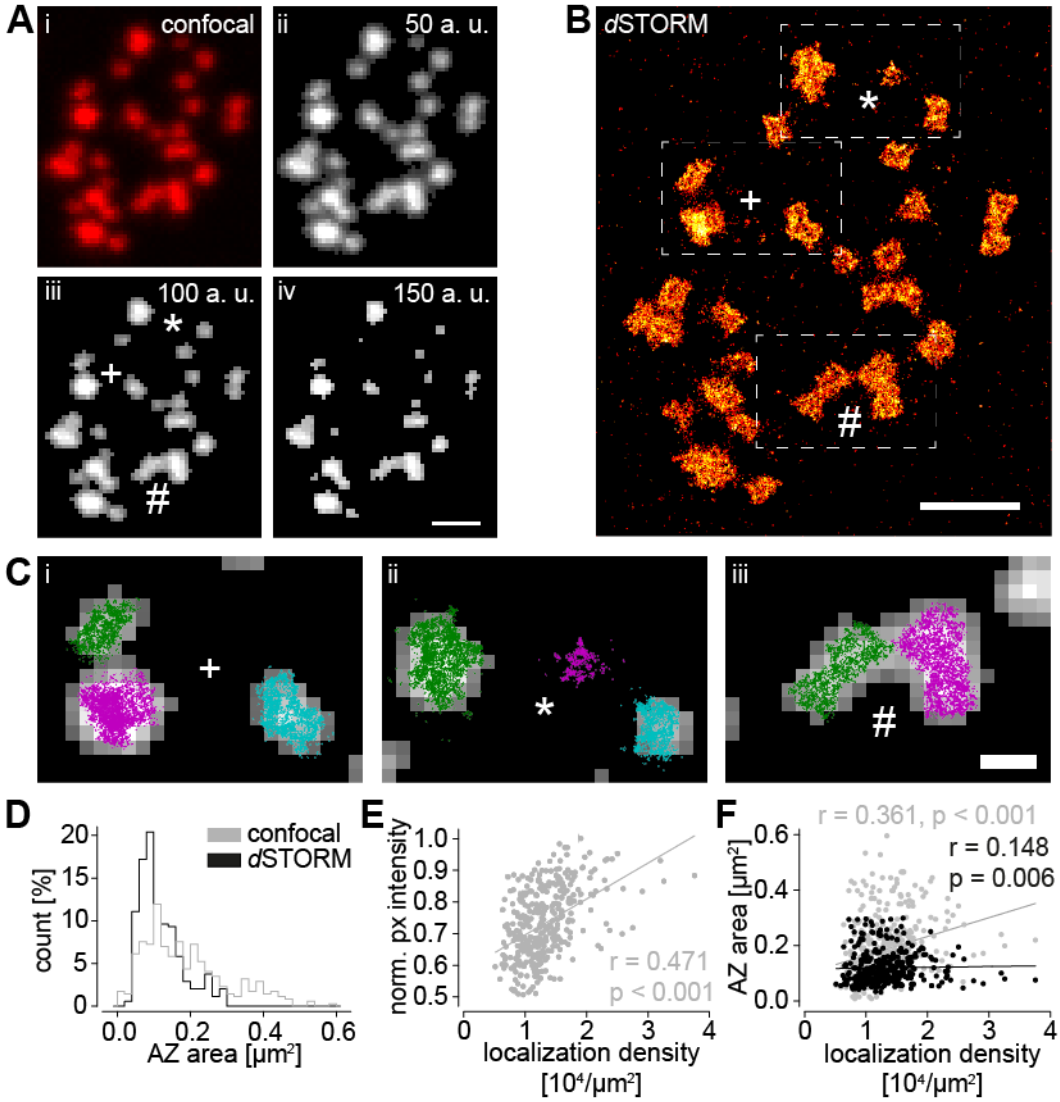

Figure 5. Correlative confocal-*d*STORM microscopy links increased localization density to increased confocal intensity and AZ area.

(A) Representative confocal image of a type Ib bouton stained as described above (see Figure 1A). (i) unprocessed original image and (ii, iii, iv) after applying an 8-bit 50, 100 and 150 a. u. threshold to the original image. Symbols mark corresponding regions in (B) enlarged in (C). Scale bar 1 µm.

(B) Representative *d*STORM image of the same bouton as shown in (A). Boxes correspond to enlarged regions in (C). Scale bar 1 µm.

(C) Enlarged confocal AZs thresholded with 100 a. u. in grey corresponding to boxed regions in (B) and overlaid scatter plots of Brp localizations from *d*STORM (green, magenta, blue for cluster identity). Localization clusters at the edges are not displayed. Scale bar 330 nm.

(D) AZ area in confocal (grey) and *d*STORM imaging (black, for D-F n = 343 corresponding AZs from 12 NMJs from 7 animals).

(E) Spearman correlation coefficient shows a positive correlation between the normalized mean pixel intensity in confocal imaging and *d*STORM localization density. (F) Spearman correlation coefficients show a much stronger correlation between AZ area in confocal imaging and localization density (grey) than in AZ area measured with *d*STORM and localization density (black).

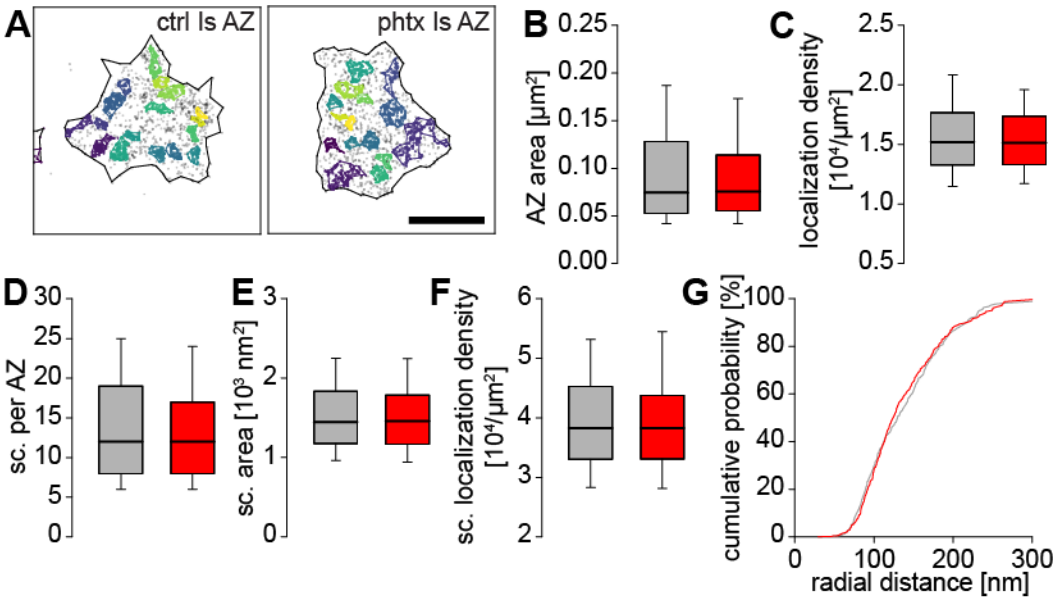

Figure 6. No further AZ compaction in type Is boutons following PhTx stimulation.

(A) Scatter plots of AZs in type Is boutons of ctrl and phtx larvae. Scale bar 200 nm.

(B, C) AZ area (B) and Brp localization density (C) in ctrl (grey, for B-G n = 449 AZs from 16 NMJs from 6 animals) and phtx (red, for B-G n = 406 AZs from 13 NMJs from 5 animals).

(D-F) Number of subclusters per AZ (D), subcluster area (E) and Brp localization density of subclusters (F) in ctrl and phtx.

(G) Cumulative plots of the radial distance between the AZ c.o.m. and the c.o.m. of individual subclusters in both groups.

SUPPLEMENTARY MATERIAL

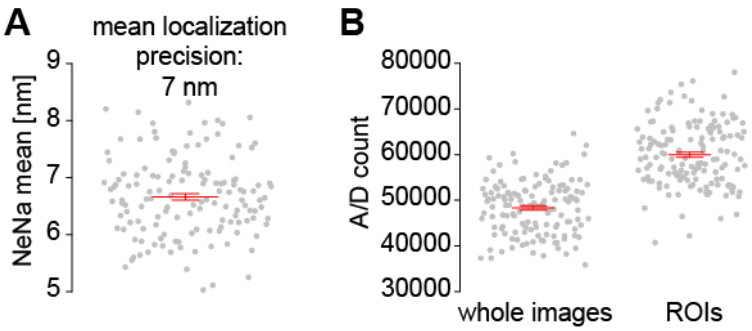

Supplementary Figure 1. Quantification of localization precision and intensity.

(A) Scatter plots of localization precision determined by NeNa algorithm. Data points (grey) correspond to single *d*STORM measurements related to Figures 1-3, 6 and Supplementary Figure 4 (for A and B). Mean localization precision (red, mean ± SEM) was 7 nm in this study.

(B) A/D counts in whole *d*STORM images and in regions of interest (ROIs) for the experimental groups. Data points for individual images (grey) as well as mean ± SEM (red) are displayed. There were no significant differences between groups.

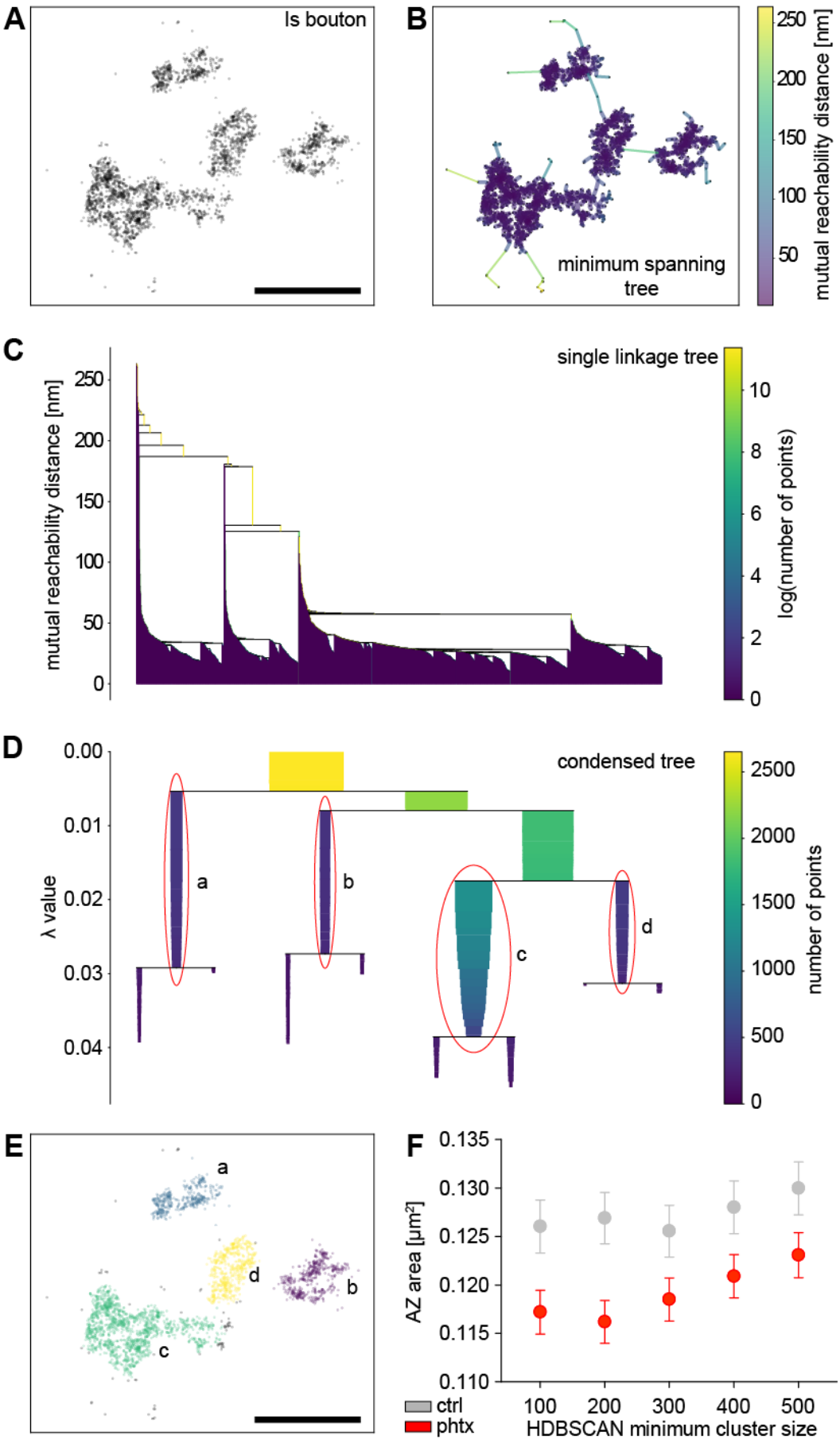

1188

1189

Supplementary Figure 2. HDBSCAN principle and robustness.

(A) Scatter plot of Brp localizations of a type Is bouton. Scale bar 500 nm.

(B) Minimum spanning tree generated with HDBSCAN in Python (minimum cluster size 100, minimum samples 25, cluster selection method ‘excess of mass’, see Material and Methods) for bouton displayed in (A). Color of the lines between nearest points indicates their respective mutual reachability distance according to the color bar.

(C) Single linkage tree computed based on the mutual reachability distance.

(D) Condensed cluster tree computed from single linkage tree based on minimum cluster size. Red circles correspond to the most robust clusters in this example and lowercase letters indicate cluster identity corresponding to (E). The λ-value is the reciprocal of the mutual reachability distance.

(E) Data from (A-D) with individual localization clusters in different colors and lowercase letters indicating cluster identity corresponding to (D). Grey points indicate unclustered localizations. Scale bar 500 nm.

(F) Scatter plots (mean ± SEM) showing the relation between varying HDBSCAN minimum cluster size for the detection of AZ clusters and AZ area with HDBSCAN minimum samples at a constant fraction of 25 % in ctrl (grey) and phtx (red) type Ib boutons of NMJs on muscles 6/7. Differences in AZ area between both groups show the same tendency independent of parameter variation and, thus, are considered to be robust. Visualization of the clustering with different parameter combinations showed similarly reliable behavior with a slight tendency to better cluster segmentation for smaller values. For the quantification throughout this manuscript the parameter combination minimum cluster size 100 and minimum samples 25 was chosen for AZ detection. Data for all parameters in this plot where equally corrected for outliers with the same thresholds (Material and Methods).

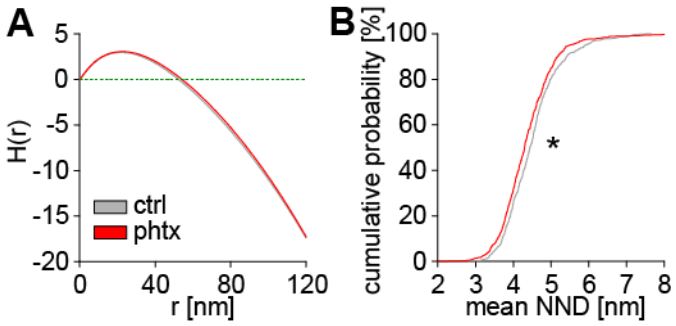

Supplementary Figure 3. H functions and nearest neighbor analysis of AZs during acute homeostatic plasticity.

(A) Averaged H functions (derivative from Ripley's K function, see Material and Methods) of all AZ localizations of ctrl (grey) and phtx (red). Positive values for H(r) indicate clustering and negative values dispersion or edge effects. Maximum positive values roughly correspond to the radius of putative AZ subclusters.

(B) Cumulative plots of the mean nearest neighbor distance of all Brp localizations per AZ in both groups (ctrl: n = 568 AZs from 13 NMJs from 6 animals; phtx: n = 792 AZs from 14 NMJs from 5 animals).

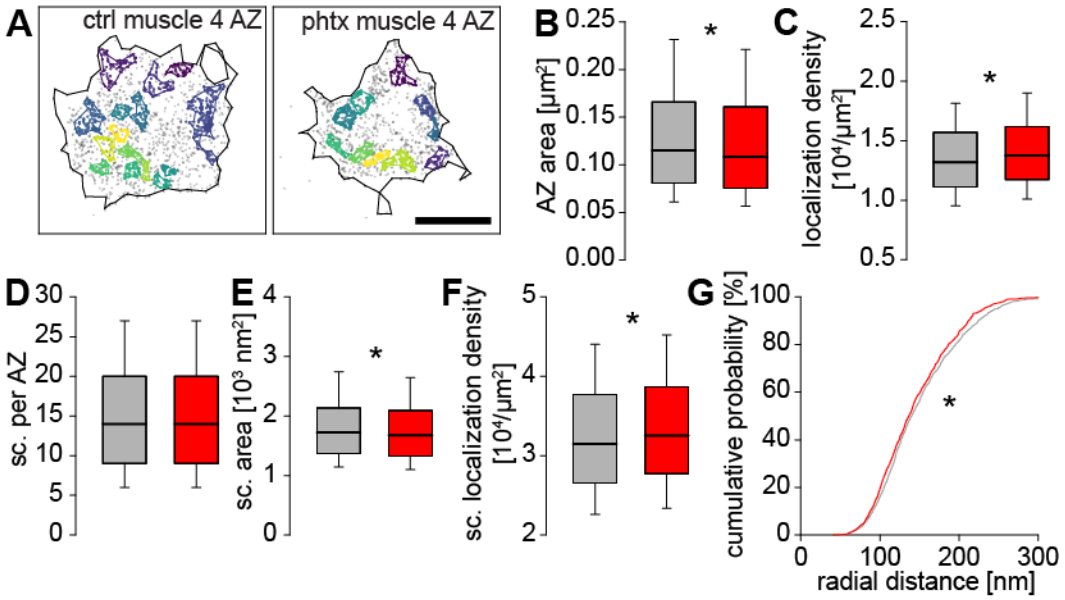

Supplementary Figure 4. AZ nanoarchitecture in type Ib boutons from NMJs on abdominal muscle 4 of *Drosophila* 3rd instar larvae.

(A) Scatter plots of a ctrl and a phtx type Ib AZ. Scale bar 200 nm.

(B, C) AZ area (B) and Brp localization density (C) in ctrl (grey, for B-G n = 1183 AZs from 20 NMJs from 6 animals) and phtx (red, for B-G n = 1445 AZs from 22 NMJs from 8 animals).

(D-F) Subcluster numbers per individual type Ib AZ (D), subcluster area (E) and subcluster localization density (F) in both groups.

(G) Cumulative plots of the radial distance between the AZ c.o.m. and the c.o.m. of individual subclusters in ctrl and phtx.

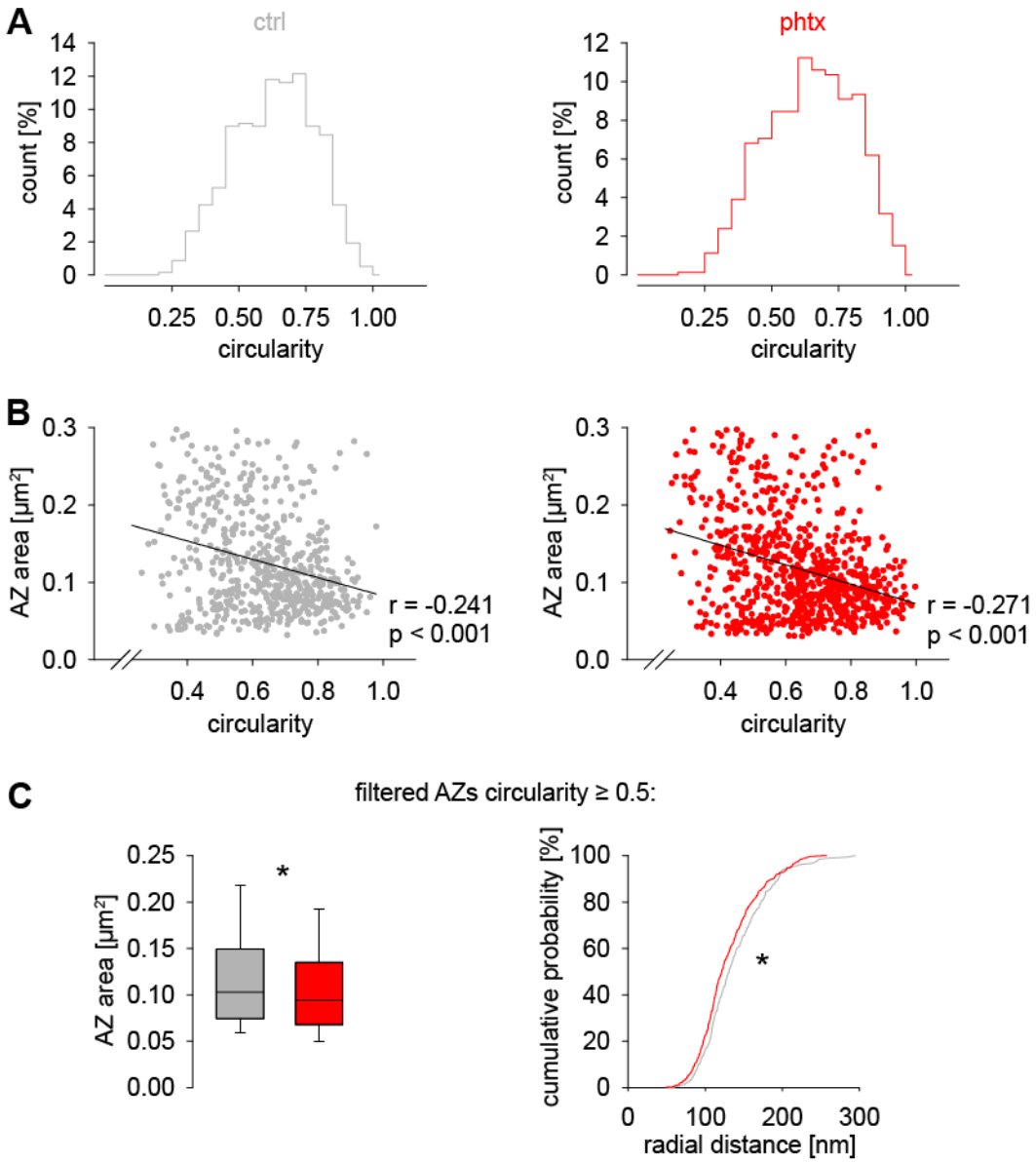

Supplementary Figure 5. AZ circularity in type Ib boutons after PhTx treatment.

(A) AZ circularity (ratio of Eigenvalues with 1.0 representing a perfect circle) in ctrl (grey, n = 568 AZs from 13 NMJs from 6 animals) and phtx (red, n = 792 AZs from 14 NMJs from 5 animals). Phtx did not change circularity of AZs (p = 0.161).

(B) Scatter plots illustrating correlation of AZ circularity and area in ctrl and phtx and linear regression curves (black lines). Spearman coefficients r and p-values show negative correlations between groups.

(C) AZs with circularity ≥ 0.5 (which was taken as indication for an AZ viewed from top) were used to compare AZ organization in ctrl and phtx. Box plots of AZ area and cumulative plots of the radial distance between the AZ c.o.m. and the c.o.m. of individual subclusters (n = 442 AZs from 13 NMJs from 6 animals and n = 621 AZs from 14 NMJs from 5 animals in ctrl and phtx, respectively).